A Unified Sampled-Data Small-Signal Model for a Ripple-Based COT Buck Converter With Arbitrary Ripple Injection Network

This article has been accepted for publication in IEEE Transactions on Circuits and Systems I: Regular Papers. This is the author's version which has not been fully edited and content may change prior to final publication. Citation information: DOI 10.1109/TCSI.2025.3557278

A Unified Sampled-Data Small-Signal Model for a Ripple-Based COT Buck Converter with Arbitrary Ripple Injection Network

Francesco Gabriele*, *Graduate Student Member, IEEE*, Antonio Carlucci*, *Graduate Student Member, IEEE*, Davide Lena, Fabio Pareschi, *Senior Member, IEEE*, Riccardo Rovatti, *Fellow, IEEE*, Stefano Grivet-Talocia, *Fellow, IEEE*, Gianluca Setti, *Fellow, IEEE*

***Abstract*—In this paper, we present a novel and unified small-signal modeling technique for Pulse-Width Modulated (PWM) DC-DC Buck converters with Ripple-Based Constant On-Time (RBCOT) control. In fact, despite the spread of RBCOT-based converters in several applications requiring tight dynamic performances and a low architectural complexity, their description through small-signal models is not always as reliable as that of fixed-frequency PWM control architectures, and a general and exact modeling framework is not well established. The proposed methodology is grounded on the DC-DC converter state-space representation and thus, differently from other modeling techniques, it permits to fully characterize the dynamic behavior of generic RBCOT converter topologies with arbitrary complex power stage and ripple injection networks. As a case study, we derive the small-signal model for a Buck converter embedding a widely used ripple injection network in industrial applications. The validity of the theoretical results is confirmed through direct comparison with SIMetrix/SIMPLIS simulations and experimental measurements in practical application scenarios, confirming the accuracy of the model even well beyond the converter switching frequency.**

***Index Terms*—RBCOT Buck Converter, PWM DC-DC Converter, Small-Signal Modeling, Sampled-Data Model**

I. Introduction

In the last few decades, Pulse-Width Modulated (PWM) Buck converters with variable-frequency Ripple-Based Constant-On-Time (RBCOT) control demonstrated to be the optimal solution for many scenarios, mostly thanks to their architectural simplicity, higher efficiency at light-loads and shorter transient response time compared to conventional Fixed-Frequency Control (FFC) architectures, e.g., Voltage and Current Mode Control (VMC and CMC, respectively). Benefits of COT control are reviewed in [4] and [1], [5]–[7].

Indeed, despite the simplicity of the architecture, whose block schematic is shown in Fig. 1(a), extracting an equivalent small-signal model is not as well consolidated as in the case of DC-DC converters featuring FFC [8]–[11]. Concerning design and analysis of DC-DC converters, small-signal models are of paramount importance from a practical engineering perspective [12]–[15] to capture the converter dynamics around a specific cyclostationary operating point so as to obtain a small-signal Linear Time-Invariant (LTI) circuit model.

The averaging technique [16]–[18] yields physical insight into the low-frequency dynamic behavior of the circuit but it intrinsically neglects the presence of a ripple signal when the averaging operator is applied. Although averaging is typically employed for designing traditional VMC converters [10], [13], [19], [20], it fails to accurately describe the RBCOT DC-DC converter dynamics in the whole frequency range because, in this case, the dynamical evolution of the RBCOT converter essentially depends on the presence of a non-negligible ripple signal. For example, a major limitation of the averaging method is that it cannot predict high-frequency effects such as subharmonic instability occurring at half-switching frequency in CMC architectures [21]–[23]. Recently, an improved averaged high-frequency model has been proposed in [24] and applied to PWM RBCOT converter, exploiting moving Fourier coefficients. Fourier series is used in [25] to provide RBCOT small-signal models considering the presence of an outer feedback loop. The sampled-data small-signal modeling techniques, firstly presented in [26], rigorously explicate the sampling effect of the converter modulator in the small-signal limit, allowing to predict fast-scale instability in the current-programmed architecture directly from a canonical small-signal model. Based on this theory, subsequent works [21], [23], [27] provide simplified and easy-to-use equivalent small-signal circuit models based on the traditional averaging technique, but additionally incorporate the sample-and-hold effect into the converter inner current loop. This enables predicting fast-scale phenomena through compact averaged small-signal models. Unfortunately, an equivalent and directly identifiable sample-and-hold effect does not exist for RBCOT converters.

The Describing Function (DF) method is used due to the quasi-linear behavior of converters [28]–[30]. RBCOT Buck converters with both current-mode and V^2 control have been modeled through the DF technique in [31], [32]. This technique has been further developed to handle feedback signals with exponentially-varying slope [33] and to extract a loop gain model for RBCOT converters [34] to investigate

F. Gabriele, A. Carlucci, F. Pareschi and S. Grivet-Talocia are with the Department of Electronics and Telecommunications, Politecnico di Torino, 10129 Torino, Italy (e-mail: {francesco.gabriele, antonio.carlucci, fabio.pareschi, stefano.grivet}@polito.it).

D. Lena is with STMicroelectronics s.r.l. – Torino, Italy. (email: davide.lena@st.com).

R. Rovatti is with the Department of Electrical, Electronic, and Information Engineering, University of Bologna, 40136 Bologna, Italy, and also with the Advanced Research Center on Electronic Systems (ARCES), University of Bologna, 40125 Bologna, Italy (e-mail: riccardo.rovatti@unibo.it).

G. Setti is with CEMSE, King Abdullah University of Science and Technology (KAUST), Saudi Arabia (e-mail: gianluca.setti@kaust.edu.sa).

* These authors contributed equally to this work.

This article has been accepted for publication in IEEE Transactions on Circuits and Systems I: Regular Papers. This is the author's version which has not been fully edited and content may change prior to final publication. Citation information: DOI 10.1109/TCSI.2025.3557278

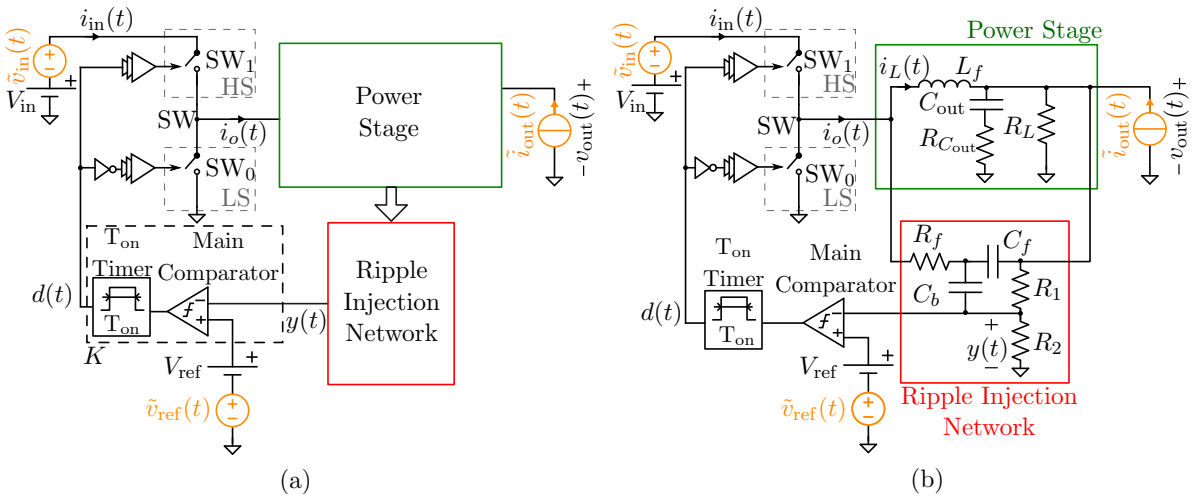

Fig. 1. DC-DC Buck converter with RBCOT control. (a) General functional block schematic of a RBCOT architecture; (b) a RBCOT Buck converter with a widely used ripple injection network ([1]–[3]).

stability and bandwidth. In [7] and [35], a DF-based modeling approach for multiphase and series capacitor trans-inductor COT regulators has been presented, respectively. In [15], [36], the DF is applied to more intricate RBCOT architectures. In all these models, RBCOT modulator, inductor and power switches are treated as a single entity since the beginning of the modeling process. Consequently, it is not possible to identify the impact that individual converter parts have, and the final results can only be used to describe a specific closed-loop transfer function (TF). Indeed, the derivation is strongly dependent on the topology analyzed and it is based on direct calculations made on the converter perturbed waveforms in time domain. Furthermore, the DF modeling technique is not easily adaptable to other RBCOT architectures [1], [37]–[40].

The sampled-data modeling approach [21], [26] has been recently extended to RBCOT converters in [6]. Focusing on the sampling characteristics of the modulator, the fundamental difference compared to FFC architectures is the number of sampling instants in each switching period: RBCOT converters take two samples (spaced apart by T_{on}, i.e., the length of the ON pulse) in a switching period rather than a single one. However, although in this case the COT modulator is separately analyzed and a compact small-signal model is provided, the expression for the static modulator gain factor F_m is introduced without a clear theoretical foundation. As it will be shown in the next sections, fixing F_m a priori results in several inaccuracies in both the modulator and the closed-loop small-signal TFs. Furthermore, the presented model is incomplete, as only the control-to-output TF is given. The derivation of other relevant features such as audio-susceptibility and output/input impedance is still lacking. These limitations hamper the establishment of a complete topology-independent modeling tool and motivate further investigations.

In this paper, we propose a novel exact small-signal modeling method aiming to develop a unified and general theory for RBCOT Buck converters. The purpose of this work is to provide an improved model of well-established RBCOT architectures. The presented technique is grounded on the converter state-space representation and it thus enables complete evaluation of the system dynamics, irrespective of its architectural complexity (i.e., it can be potentially exploited to determine any TF of an RBCOT converter with arbitrarily intricate circuit networks). Differently from the pioneering works in [6], [31], [32], the complete modulator small-signal model is derived without either invoking in advance the modulator sampling characteristics or fixing the expression of F_m. Furthermore, the derivation process does not require any assumptions on the time-domain converter evolution in response to external perturbations. In fact, both the final structure of the small-signal model and the F_m expression turn out to be a *by-product* of the detailed methodology and need not be assumed beforehand. As a concrete application example, the proposed modeling technique is validated by considering the RBCOT architecture shown in Fig. 1(b), which is a DC-DC converter topology widely used in industrial applications [1]–[3]. To the best of the authors' knowledge, an exact and complete small-signal model for this RBCOT converter has never been derived up to now. The validation process is conducted through the use of the SIMPLIS simulator engine. Specifically, an `.AC` analysis of the RBCOT converter operating in a Periodic Operating Point (`.POP`) is performed, allowing for a comparison between the simulated frequency response and the results derived from the proposed analytical model. A detailed comparison between the proposed modeling method and the ones in [6], [31], [32], [34] is also conducted.

The paper is organized as follows. After formalizing the problem of TF computation in Sec. II, we proceed with the main developments in Sec. III, where the closed-form analytical expressions of the main small-signal TFs embedding the converter sampling process are derived. Based on these fundamental results, a complete converter small-signal model is provided in Sec. IV. Then, practical application examples and a comparison with other modeling techniques are discussed in Sec. V. Finally, we draw the conclusions.

II. Problem statement and notation

A general architecture for a RBCOT Buck converter is shown in Fig. 1(a). The fixed input voltage $V_{\rm in}$ is chopped through the action of the High-Side (HS) and Low-Side (LS) switches $\mathrm{SW}_{0,1}$, both driven by a control signal $d(t)$. The signal produced on the SW node is applied to a Power Stage. This includes the converter output filter generating the desired output voltage level $V_{\rm out}$ (see, for instance, Fig. 1(b), where a typical LC filter made up by the elements L_f, $C_{\rm out}$ and $R_{C_{\rm out}}$ is employed). From the Power Stage, a set of signals is sensed and sent to the Ripple Injection Network, which synthesizes a feedback signal $y(t)$. This signal might be directly extracted from the Power Stage (e.g. it might be the inductor current $i_L(t)$ or the output voltage $v_{\rm out}(t)$) or, alternatively, it can stem from a more complex circuit network, such as the one in Fig. 1(b). The signal $y(t)$, featuring a certain switching ripple, determines the time evolution of the RBCOT converter. Indeed, a *modulator* K senses a feedback signal $y(t)$ and produces a pulse whenever it reaches a certain reference threshold value $V_{\rm ref}$. The main feature of switching converters with RBCOT control is that the feedback loop produces a control signal $d(t)$ consisting in a sequence of rectangular pulses of fixed duration $T_{\rm on}$, generated by a $\mathrm{T_{on}}$ Timer. To formalize this behavior, we introduce the time instants t_k, indexed by $k \in \mathbb{Z}$, to denote the time when the k-th pulse begins. This sequence satisfies

$$y(t_k) = V_{\rm ref}, \quad \forall\, k \in \mathbb{Z} \tag{1}$$

and the duty cycle control signal is thus a sequence a pulses starting at t_k,

$$d(t) = \sum_{k\in\mathbb{Z}} p_{T_{\rm on}}(t - t_k) \tag{2}$$

where $p_{T_{\rm on}}(t) = 1$ if $0 \le t \le T_{\rm on}$ and zero otherwise.

Throughout this paper, we adopt the notation that lowercase letters indicate network quantities (e.g. in Fig. 1, $v_{\rm out}$, $i_{\rm in}$, d, etc.) that are typically time-varying. Their capitalized versions denote constant values (e.g. $V_{\rm in}$ and $V_{\rm ref}$ are the values of the DC component of the input and reference voltages, respectively). A barred letter like $\bar{q}(t)$ denotes the steady-state response of the variable q in periodic steady-state operation, when no perturbation is applied and external excitations are kept constant. When perturbations are applied to the network sources for the sake of computing TFs, the symbol $\tilde{q}$ denotes the (small-signal) deviation of q from the unperturbed steady-state $\bar{q}(t)$, i.e. there is a decomposition $q(t) = \bar{q}(t) + \tilde{q}(t)$.

By analogy and in accordance with the standard definition, the small-signal TF H_u^w from an independent excitation u to a network variable w (e.g. output voltage, duty cycle signal, etc.) links the first-order response $\tilde{w}(t)$ due to a harmonic excitation

$$\tilde{u}(t) = a\cos\omega_p t \tag{3}$$

at a given frequency ω_p, and the corresponding Fourier component of the input $\tilde{u}(t)$. In particular, we consider that the COT converter works around a periodic operating point, corresponding to constant $V_{\rm in}$, $I_{\rm out}$, $V_{\rm ref}$, with period T so that any given network variable w has a periodic response $\bar{w}(t)$ when no small-signal perturbation is applied. Upon applying the perturbation $\tilde{u}(t)$, the response becomes $w(t) = \bar{w}(t) + \tilde{w}(t)$. It is assumed that the *small-signal response* $\tilde{w}(t)$ is quasi-periodic with a discrete frequency spectrum. In particular, since there are two periodic input signals involved, the response will be exactly periodic only if the periods T and $T_p = 2\pi/\omega_p$ have a common multiple or, in other words, only if there are two positive integers ℓ_1,ℓ_2 such that $\ell_1 T_p = \ell_2 T$. Following the theory of describing functions [29], we focus on the fundamental harmonic component at the same frequency ω_p as the driving input, that we denote $[w]_1$. We adopt the following definition of TF $H_u^w(\mathrm{j}\omega_p)$ from the excitation u to the output quantity w,

$$H_u^w(\mathrm{j}\omega_p) = \lim_{a\to 0} \left.\frac{[\tilde{w}]_1}{a/2}\right|_{\tilde{u}(t)=a\cos\omega_p t}. \tag{4}$$

In words, the TF value at $\mathrm{j}\omega_p$ is found by exciting the system with the harmonic disturbance $\tilde{u}$ in (3) and then considering the gain from this input to the fundamental (i.e., the spectral component at the same input frequency ω_p) Fourier coefficient of the response $\tilde{w}(t)$ as the amplitude $a \to 0$ (small-signal conditions).

The circuit topology used in our analysis is depicted in Fig.1(a). The filtering stage following the power switches is regarded as an LTI circuit, denoted as G, driven by the voltage $v_{\rm SW}(t) = d(t)v_{\rm in}(t)$ at the SW node, where $v_{\rm in}(t) = V_{\rm in} + \tilde{v}_{\rm in}(t)$. Taking this linear sub-network aside, it is useful to consider its TF $G(s) \equiv H^y_{v_{\rm SW}}(s)$ from $v_{\rm SW}$ to the feedback signal y. Following the state-space approach of [26], G can be represented as

$$G: \begin{cases} \dot{\boldsymbol{x}} = \mathbf{A}\boldsymbol{x} + \boldsymbol{b}dv_{\rm in} \\ y = \boldsymbol{c}\boldsymbol{x} \end{cases} \tag{5}$$

where $\mathbf{A} \in \mathbb{R}^{\nu\times\nu}$ is the state matrix and $\boldsymbol{x} \in \mathbb{R}^\nu$ is the hidden state vector, $\boldsymbol{b} \in \mathbb{R}^\nu$ is a column vector, $\boldsymbol{c} \in \mathbb{R}^\nu$ is a row vector. Equation (5) combined with (2) defining d and, most importantly, with the implicit condition (1) defining the switching instants t_k form a complete description of the COT converter that, in principle, could be solved to find the response y. Note that, differently from other approaches [6], [31], [32] where the derivation of the small-signal TF is strongly reliant on a priori approximations of the time-domain waveform of y (linear or parabolic), we do not make simplifying assumptions on the network G at this stage. This arbitrariness allows us to address several topologies at once, including traditional V^2 COT control architectures [31], [32], [41] and more advanced COT topologies adopted in industry applications [2], [3].

In the following sections we will need to evaluate the response y to a given signal $d(t)v_{\rm in}(t)$, i.e. the output of the system (5). To this aim it is useful to recall that, if the state at some initial time t_0 is $\boldsymbol{x}(t_0)$, then the well-known convolution formula gives the state at a later time t,

$$\boldsymbol{x}(t) = e^{\mathbf{A}(t-t_0)}\boldsymbol{x}(t_0) + \int_{t_0}^{t} e^{\mathbf{A}(t-\tau)}\boldsymbol{b}d(\tau)v_{\rm in}(\tau)d\tau \tag{6}$$

In case the input signal is defined for all times,

$$\boldsymbol{x}(t) = \int_{-\infty}^{t} e^{\mathbf{A}(t-\tau)}bd(\tau)v_{\rm in}(\tau)d\tau \tag{7}$$

Similarly, the feedback variable is $y(t) = \int_{-\infty}^{t} g(t-\tau)d(\tau)v_{\rm in}(\tau)d\tau$, where $g(\tau) = \boldsymbol{c}e^{\mathbf{A}\tau}\boldsymbol{b}$ is the impulse response.

Throughout this paper, we use boldface capital letters ($\mathbf{X}$) to indicate matrices and lowercase letters for vectors ($\boldsymbol{x}$). We use the symbol $\mathbb{I}$ to indicate the identity matrix, the letter $\delta(\cdot)$ for Dirac's delta distribution, and j for the imaginary unit. The transpose of a matrix $\mathbf{X}$ is $\mathbf{X}^{\rm T}$. We also use the matrix exponential $e^{\mathbf{X}} \triangleq \sum_{k=0}^{\infty}(k!)^{-1}\mathbf{X}^k$ (see [42]).

III. Derivation

A. Preliminaries: Periodic steady-state operation

In steady-state conditions, we can define the time axis to conveniently have the switching instant $\bar{t}_0 = 0$. With this choice, we have $\bar{t}_k = kT$ and $\bar{\boldsymbol{x}}(\bar{t}_0) = \bar{\boldsymbol{x}}(0) \triangleq \boldsymbol{x}_0$. Periodicity implies that, at the beginning of every switching period, the internal state is the same so that $\bar{\boldsymbol{x}}(\bar{t}_k) = \boldsymbol{x}_0$. Therefore, (6) applied to the interval $[0, T]$ implies that the $\boldsymbol{x}_0$ and T must satisfy the following periodicity condition

$$e^{\mathbf{A}T}\boldsymbol{x}_0 + \int_0^{T_{\rm on}} e^{\mathbf{A}(T-\tau)}\boldsymbol{b}V_{\rm in}\,{\rm d}\tau = \boldsymbol{x}_0 \tag{8}$$

together with the COT control law (1), that in this context reads

$$\bar{y}(\bar{t}_k) = \boldsymbol{c}\boldsymbol{x}_0 = V_{\rm ref}. \tag{9}$$

In periodic steady-state operation no external disturbances are applied to the system, i.e., $\tilde{v}_{\rm in}(t) = \tilde{v}_{\rm ref}(t) = 0$. Therefore, equations (8) and (9) can be solved simultaneously for the period T and the state $\boldsymbol{x}_0$ to characterize the unperturbed, steady-state operation. In particular, solving for $\boldsymbol{x}_0$ in (8) yields

$$\boldsymbol{x}_0 = -\mathbf{A}^{-1}(\mathbb{I} - e^{-\mathbf{A}T})^{-1}(\mathbb{I} - e^{-\mathbf{A}T_{\rm on}})\boldsymbol{b}V_{\rm in}. \tag{10}$$

B. Control-to-duty TF

Let us now consider the closed-loop response to a small signal disturbance $\tilde{v}_{\rm ref}(t) = a\cos\omega_p t$ on top of the reference value $V_{\rm ref}$. Applying $\tilde{v}_{\rm ref}(t)$ causes the circuit to deviate from the steady-state conditions discussed in Sec. III-A and, as depicted in Fig. 2, each switching instant t_k will be delayed or anticipated by an amount $\tilde{t}_k$ compared to the steady-state $\bar{t}_k$,

$$t_k = \bar{t}_k + \tilde{t}_k. \tag{11}$$

These deviations are such that the COT control law (1) is fulfilled

$$y(\bar{t}_k + \tilde{t}_k) = V_{\rm ref} + \underbrace{a\cos[\omega_p(\bar{t}_k + \tilde{t}_k)]}_{\tilde{v}_{\rm ref}(t_k)}, \qquad \forall\ k \in \mathbb{Z} \tag{12}$$

Similarly, the duty cycle signal becomes $d(t) = \bar{d}(t) + \tilde{d}(t)$, where the difference $\tilde{d}(t) = d(t) - \bar{d}(t)$ is a sequence of pulses of duration $\tilde{t}_k$ with every positive pulse followed by a negative pulse distanced by $T_{\rm on}$ (see Fig. 2, bottom), that is

$$\tilde{d}(t) = \sum_{k=-\infty}^{+\infty} -p_{\tilde{t}_k}(t - \bar{t}_k) + p_{\tilde{t}_k}(t - T_{\rm on} - \bar{t}_k) \tag{13}$$

This equation is clarified in Fig. 2, which shows that, upon applying this disturbance on the reference level $V_{\rm ref}$ (top panel, orange line), the intercept with the signal $y(t)$ are shifted. A positive $\tilde{t}_k$ implies that the $T_{\rm on}$ pulse is delayed (Fig. 2, middle) meaning that d lags with respect to $\bar{d}$. This implies that the difference $\tilde{d}(t) = d(t) - \bar{d}(t)$ with respect to the steady state includes a negative pulse at $\bar{t}_k$ of width $\tilde{t}_k$ followed by a positive one later after the on-time $T_{\rm on}$ (Fig. 2, bottom). Vice versa, a negative $\tilde{t}_k$ signifies that the $T_{\rm on}$ pulse leads with respect to the steady state.

We see that, given the switching instants t_k, the signal $d(t)$ is defined and, consequently, the evolution of G in (5) is entirely determined. Moreover, the response y at time t_k only depends on the earlier values t_n, with $n \le k$. Therefore, we can think of y as a function $y(t_k) = y(t_k; \{t_n\}_{n\le k}, a)$ of the switching instants $\{t_n\}_{n\in\mathbb{Z}}$ that define the signal $d(t)$. With this notation, condition (12) becomes

$$y(t_k; \{t_n\}_{n\le k}, a) = V_{\rm ref} + a\cos\omega_p t_k, \qquad \forall\, k \in \mathbb{Z}. \tag{14}$$

Since for a given value of disturbance amplitude a the perturbed switching instants must solve (14), the unknown sequence of switching instants $t_k = t_k(a)$ can be considered a function of a implicitly defined as the solution of (14). In a small-signal analysis, we are interested in the behavior of this sequence for small a. Note that, for $a = 0$, the solution is the steady-state with $t_k = \bar{t}_k$ and $\tilde{t}_k = 0$. When $a \to 0$, we can look at how the solution sequence t_k is affected by implicitly differentiating (14) with respect to a and evaluating the derivatives at $a = 0$ to obtain

$$\alpha\xi_k + \sum_{m=-\infty}^{k-1} \beta_{k-m}\xi_m = \cos\omega_p\bar{t}_k, \qquad \forall k \in \mathbb{Z} \tag{15}$$

where the coefficients α and β_{k-m} arise from using the chain rule for derivatives, and ξ_m is the sequence we need to solve for. These are defined as

$$\alpha = \left.\frac{\partial y(t_k; \{t_n\}_{n\le k}, a)}{\partial t_k}\right|_{a=0, t_n=\bar{t}_n} \tag{16a}$$

$$\beta_{k-m} = \left.\frac{\partial y(t_k; \{t_n\}_{n\le k}, a)}{\partial t_m}\right|_{a=0, t_n=\bar{t}_n} \tag{16b}$$

$$\xi_m = \left.\frac{\partial t_m}{\partial a}\right|_{a=0} \tag{16c}$$

Note that, in the above, we have tacitly assumed the existence of the derivatives of $t_k(a)$ around zero. Explicit expressions of (16) are postponed to the next section, where it will become evident why α is indeed independent of k and β only depends on the difference $k - m$, both because of periodicity of the steady-state operating point around which the system is perturbed.

Equation (15) is a linear recurrence in ξ_k solvable, for instance, via z-transform techniques. We remark that, by linearity, we are only interested in the forced response due to the terms on the right hand side of (15). Thus, we directly seek a steady-state solution of the form

$$\xi_k = {}^1\!/_2\,\Xi(e^{{\rm j}\omega_p T})e^{{\rm j}\omega_p kT} + {}^1\!/_2\,\Xi(e^{-{\rm j}\omega_p T})e^{-{\rm j}\omega_p kT} \tag{17}$$

Substituting (17) into (15) and rearranging gives a linear combination of $e^{{\rm j}\omega_p kT}$ and $e^{-{\rm j}\omega_p kT}$ that must identically

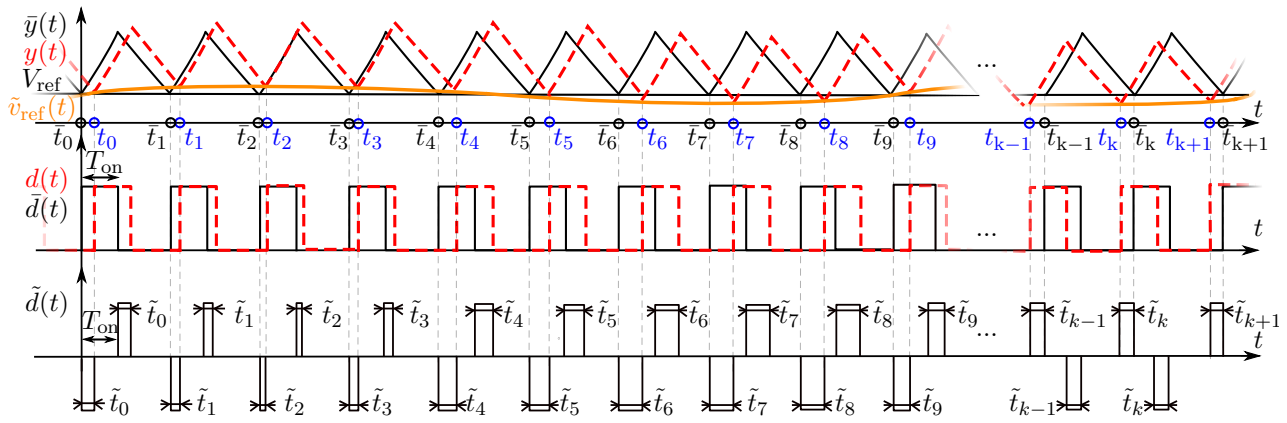

Fig. 2. Waveforms of duty cycle $d(t)$ and control signal $y(t)$ in steady-state and perturbed conditions. The fixed reference voltage $V_{\rm ref}$ is perturbed with a sinusoidal orange excitation.

vanishing for all k, implying that the coefficients multiplying the two exponentials must be zero, i.e.

$$\Xi\left(e^{\pm \mathrm{j}\omega_p T}\right)\left[\alpha + \sum_{m=-\infty}^{k-1} \beta_{k-m} e^{\pm \mathrm{j}\omega_p (m-k)T}\right] - 1 = 0. \quad (18)$$

Solving for $\Xi(e^{\mathrm{j}\omega_p t})$ finally yields

$$\Xi(e^{\mathrm{j}\omega_p T}) = [\alpha + e^{-\mathrm{j}\omega_p T} B(e^{\mathrm{j}\omega_p T})]^{-1} \quad (19)$$

where $B(z) = \sum_{k=0}^{\infty} \beta_{k+1} z^{-k}$ is the unilateral z-transform of the sequence $\{\beta_{k+1}\}_{k=0}^{\infty}$.

In order to find the control-to-duty TF $H^d_{v_{\rm ref}}(\mathrm{j}\omega_p)$, we should look at the spectrum of $\tilde{d}(t)$ according to the definition (4).

The Fourier transform of $\tilde{d}(t)$ in (13) is

$$\hat{d}(\mathrm{j}\omega) = \frac{1}{2\pi} \sum_{k=-\infty}^{+\infty} -\frac{e^{-\mathrm{j}\omega \bar{t}_k}}{\mathrm{j}\omega}(1 - e^{-\mathrm{j}\omega \tilde{t}_k})(1 - e^{-\mathrm{j}\omega T_{\rm on}}) \quad (20)$$

Using the equality $\lim_{a\to 0} (1 - e^{-\mathrm{j}\omega \tilde{t}_k})/a = \mathrm{j}\omega \frac{\partial \tilde{t}_k}{\partial a} = \mathrm{j}\omega \xi_k$ in (20), we get

$$\hat{d}_0(\mathrm{j}\omega) \triangleq \lim_{a\to 0} \frac{\hat{d}(\mathrm{j}\omega)}{a/2} = -\frac{1}{2\pi} \sum_{k=-\infty}^{+\infty} 2\xi_k (1 - e^{-\mathrm{j}\omega T_{\rm on}}) e^{-\mathrm{j}\omega k T} \quad (21)$$

Using (17) combined with Poisson's summation formula,

$$\hat{d}_0(\mathrm{j}\omega) = -\frac{1}{T} \sum_{k=-\infty}^{\infty} \Xi(e^{\mathrm{j}\omega_p T})[1 - e^{-\mathrm{j}\omega T_{\rm on}}] \delta\left(\omega - \omega_p - k\frac{2\pi}{T}\right)$$
$$- \frac{1}{T} \sum_{k=-\infty}^{\infty} \Xi(e^{-\mathrm{j}\omega_p T})[1 - e^{-\mathrm{j}\omega T_{\rm on}}] \delta\left(\omega + \omega_p - k\frac{2\pi}{T}\right) \quad (22)$$

We see that the spectrum $\hat{d}_0(\mathrm{j}\omega)$ is made of discrete spectral lines, with these two summations corresponding to $\pm\omega_p$, respectively arising from the two spectral components in (17). We are interested in the component $[\tilde{d}_0]_1$ at the same frequency ω_p as the excitation, defined as the coefficient of the $k = 0$ term in the first series in (22),

$$[\tilde{d}_0]_1 = -\frac{1}{T} \Xi(e^{\mathrm{j}\omega_p T})(1 - e^{-\mathrm{j}\omega_p T_{\rm on}}) \quad (23)$$

Finally, using (19), we find the closed-form solution for $[\tilde{d}_0]_1$, which coincides with the control-to-duty TF,

$$H^d_{v_{\rm ref}}(\mathrm{j}\omega_p) = -\frac{1}{T} \frac{1 - e^{-\mathrm{j}\omega_p T_{\rm on}}}{\alpha + e^{-\mathrm{j}\omega_p T} B(e^{\mathrm{j}\omega_p T})} \quad (24)$$

C. Coefficient computations

In this section, we report the calculations to obtain the coefficients (16), that are the derivatives giving the sensitivity of the solution y to infinitesimal changes in the individual switching instants t_m. Starting with the definition (16a), the computation of α consists in finding the effect of a small perturbation $\tilde{t}_k$ around $\bar{t}_k$. Hence, in this case $y(t_k; \{t_n\}_{n<k}, a)$ is the response of G when the duty cycle control $d(t) = \bar{d}(t) + \tilde{d}(t)$ is perturbed with a pair of pulses of duration $\tilde{t}_k$, that is $\tilde{d}(t) = -p_{\tilde{t}_k}(t - \bar{t}_k) + p_{\tilde{t}_k}(t - \bar{t}_k - T_{\rm on})$.

Since all t_n are unperturbed except for $n = k$ (i.e. it holds $\tilde{d}(t) = 0, \forall\, t < \bar{t}_{k-1}$), the state response $\boldsymbol{x}(t)$ is equal to the steady state up to the instant $t = \bar{t}_{k-1}$, and we have $\boldsymbol{x}(t_{k-1}) = \boldsymbol{x}_0$. Using (6) in the interval $[\bar{t}_{k-1}, t_k]$ (with $t_k > \bar{t}_{k-1} + T_{\rm on}$),

$$\boldsymbol{x}(t_k) = e^{\mathbf{A}(t_k - \bar{t}_{k-1})} \boldsymbol{x}_0 + \int_{\bar{t}_{k-1}}^{t_k} e^{\mathbf{A}(t_k - \bar{t}_{k-1})} \boldsymbol{b} V_{\rm in}\, \mathrm{d}\tau \quad (25)$$

The derivative with respect to t_k, evaluated at $t_n = \bar{t}_n, \forall\, n$ is

$$\left.\frac{\partial \boldsymbol{x}(t_k)}{\partial t_k}\right|_{a=0, t_n = \bar{t}_n} = \mathbf{A}\boldsymbol{x}_0 \quad (26)$$

and the coefficient

$$\alpha = \boldsymbol{c}\mathbf{A}\boldsymbol{x}_0 = \dot{\bar{y}}(\bar{t}_k^-) \quad (27)$$

is the slope of the steady-state response $\bar{y}(t)$ evaluated to the left of the switching instant. This follows from the fact that, at $t = \bar{t}_k^-$, the state equation (5) is $\dot{\boldsymbol{x}}(t) = \mathbf{A}\boldsymbol{x}(t)$, hence $\mathbf{A}\boldsymbol{x}_0 = \dot{\boldsymbol{x}}(\bar{t}_k^-)$.

As for the β_k in (16b), we should consider the effect of perturbing the m-th switching instant $\bar{t}_m$ by an amount $\tilde{t}_m$ at a later observation time $\bar{t}_k$, with $k > m$. This change in the switching instant is a perturbation on the duty cycle signal $\tilde{d}_{\tilde{t}_m}(t) = -p_{\tilde{t}_m}(t - \bar{t}_m) + p_{\tilde{t}_m}(t - T_{\rm on} - \bar{t}_m)$. This is an input to

the subnetwork G defined in (5). Hence its effect on the output can be found again via the convolution formula as follows

$$\begin{aligned}\tilde{y}_{\tilde{t}_m}(\bar{t}_k) &= \int_{-\infty}^{\bar{t}_k} g(\bar{t}_k-\tau)\tilde{d}_{\tilde{t}_m}(\tau)\mathrm{d}\tau = \\ &= \boldsymbol{c}\int_{\bar{t}_{m-1}}^{\bar{t}_k} e^{\mathbf{A}(\bar{t}_k-\tau)}\boldsymbol{b}V_{\mathrm{in}}\tilde{d}_{\tilde{t}_m}(\tau)\,\mathrm{d}\tau\end{aligned} \tag{28}$$

Note that we have already isolated the perturbation response $\tilde{y}(t)$, removing terms associated with $\bar{y}(t)$. Using the definition of β_{k-m}, we get

$$\beta_{k-m} = \lim_{\tilde{t}_m\to 0}\frac{\tilde{y}_{\tilde{t}_m}(\bar{t}_k)}{\tilde{t}_m} = \boldsymbol{c}e^{\mathbf{A}(k-m)T}[e^{-\mathbf{A}T_{\mathrm{on}}}-I]\boldsymbol{b}V_{\mathrm{in}} \tag{29}$$

This equality can be explained by considering that the limit of the pulsed function $d_{\tilde{t}_m}(\tau)/\tilde{t}_m$ as $\tilde{t}_m\to 0$ in the distributional sense is a pair of Dirac's deltas $\delta(t-\bar{t}_m)-\delta(t-T_{\mathrm{on}}-\bar{t}_m)$. Hence, the integration and limit in (28)-(29) can be interpreted as a sampling operation on the impulse response $g(t)$ that results in $\beta_k = -g(kT)+g(kT-T_{\mathrm{on}})$.

Using the closed-form expression of β in eq. (29), the function $B(z)$ can be found explicitly by means of the geometric series identity, as follows

$$B(z) = \boldsymbol{c}e^{\mathbf{A}T}[\mathbb{I}-e^{\mathbf{A}T}z^{-1}]^{-1}[e^{-\mathbf{A}T_{\mathrm{on}}}-\mathbb{I}]\boldsymbol{b}V_{\mathrm{in}} \tag{30}$$

At this point we can consider the behavior of the TF (24) at DC, i.e. as $\omega_p\to 0$, where the denominator becomes $\alpha+B(1)$. By comparing (30) and (10), we see that

$$\alpha = \boldsymbol{c}\mathbf{A}\boldsymbol{x}_0 = -B(1).$$

This means that the numerator zero in the origin *cancels out* with a pole at the same frequency, thus making the control-to-duty TF finite and non-zero at $\omega_p = 0$. This can be made apparent by manipulating (24) using the identity (10) to obtain the alternative expression

$$H^d_{v_{\mathrm{ref}}}(\mathrm{j}\omega_p) = -\frac{1}{T}\frac{1-e^{-\mathrm{j}\omega_p T_{\mathrm{on}}}}{(e^{\mathrm{j}\omega_p T}-1)\boldsymbol{c}\mathbf{A}[e^{\mathrm{j}\omega_p T}\mathbb{I}-e^{\mathbf{A}T}]^{-1}\boldsymbol{x}_0} \tag{31}$$

Here, the presence of a pole at $\omega_p = 0$ is evident. This result is important because previous modeling techniques such as [6], [31], [32] are inherently dependent on the straight-line approximation as an assumption made at the beginning of the analysis. This invariably leads to a control-to-duty transfer with a spurious zero in the origin $\omega_p = 0$.

Another important observation concerns the practical computation of $B(z)$. This is straightforward when the pole-residue form of the TF $G(s) = \boldsymbol{c}(s\mathbb{I}-\mathbf{A})^{-1}\boldsymbol{b}V_{\mathrm{in}}$ is available,

$$G(s) = \sum_{i=1}^{\nu} r_i(s-p_i)^{-1} \tag{32}$$

In this case we can introduce a modal realization of $G(s)$, i.e. $\mathbf{A}\in\mathbb{C}^{\nu\times\nu}$, $\boldsymbol{b}\in\mathbb{C}^{\nu}$, $\boldsymbol{c}\in\mathbb{C}^{\nu}$ with

$$\mathbf{A} = \mathrm{diag}\{p_1,\dots,p_\nu\},\ \boldsymbol{b} = \begin{pmatrix} r_1 & \cdots & r_\nu\end{pmatrix}^{\mathrm{T}},\quad \boldsymbol{c} = \begin{pmatrix}1 & \cdots & 1\end{pmatrix}, \tag{33}$$

to be inserted in (30). Through algebraic manipulations, this gives

$$B(z) = \sum_{i=1}^{\nu}\frac{r_i e^{p_i T}}{1-e^{p_i T}z^{-1}}(e^{-p_i T_{\mathrm{on}}}-1) \tag{34}$$

which is an expression of $B(z)$, and therefore of the control-to-duty TF $H^d_{v_{\mathrm{ref}}}$ in terms of poles and residues of the linear network G following the power switches.

D. Line-to-Duty TF

The ideas outlined in the above Sec. III-B can be re-used to obtain the TF $H^d_{v_{\mathrm{in}}}$ from the input voltage v_{in} to the duty cycle d. In this case the perturbation $\tilde{v}_{\mathrm{in}}(t) = a\cos(\omega_p t)$ is injected on input voltage so that $v_{\mathrm{in}}(t) = V_{\mathrm{in}}+\tilde{v}_{\mathrm{in}}(t)$. As discussed above, this implies a perturbation of the switching instants that translates in a deviation $\tilde{d}(t)$ on the duty cycle signal. Therefore, the state equation (5) now reads

$$\dot{\boldsymbol{x}} = \mathbf{A}\boldsymbol{x}+\boldsymbol{b}[\bar{d}(t)+\tilde{d}(t)]\cdot[V_{\mathrm{in}}+a\cos(\omega_p t)]. \tag{35}$$

Here, $\tilde{v}_{\mathrm{in}}(t)$ depends directly on the amplitude a, while $\tilde{d}(t)$ depends on $\tilde{t}_k$ only. In this case the COT control law that implicitly defines the t_k is $y(t_k;\{t_n\}_{n\le k},a) = V_{\mathrm{ref}}$. Implicit differentiation with respect to a leads to

$$\alpha\xi_k + \sum_{m=-\infty}^{k-1}\beta_{k-m}\xi_m + \gamma_k = 0 \tag{36}$$

that is the counterpart of (15) where the right hand side is zero because there is no disturbance on V_{ref}, and the new coefficient γ_k is defined as

$$\gamma_k = \left.\frac{\partial y(t_k;\{t_n\},a)}{\partial a}\right|_{a=0,t_n=\bar{t}_n}. \tag{37}$$

This encodes the sensitivity of the output y to small variations of a. It can be expressed as the derivative with respect to a of the convolution integral that gives the response y,

$$\gamma_k = \int_{-\infty}^{\bar{t}_k}\boldsymbol{c}e^{\mathbf{A}(\bar{t}_k-\tau)}\boldsymbol{b}\bar{d}(\tau)\frac{e^{\mathrm{j}\omega_p\tau}+e^{-\mathrm{j}\omega_p\tau}}{2}\,\mathrm{d}\tau \tag{38}$$

The sequence γ_k represents the forcing term for the recurrence (36), and also in this case it can be recast as the superposition of two quasi-periodic geometric sequences. In fact, from (38),

$$\gamma_k = {}^1\!/_2\Gamma(\mathrm{j}\omega_p)e^{\mathrm{j}\omega_p kT}+{}^1\!/_2\Gamma(-\mathrm{j}\omega_p)e^{-\mathrm{j}\omega_p kT}. \tag{39}$$

The coefficient $\Gamma(\mathrm{j}\omega_p)$ arises from (38) through the evaluation of a definite integral resulting in

$$\Gamma(\mathrm{j}\omega_p) = -\boldsymbol{c}\mathbf{A}_{\omega_p}^{-1}[e^{-\mathbf{A}_{\omega_p}T}-\mathbb{I}]^{-1}[e^{-\mathbf{A}_{\omega_p}T_{\mathrm{on}}}-\mathbb{I}]\boldsymbol{b} \tag{40}$$

where $\mathbf{A}_{\omega_p}\triangleq\mathbf{A}-\mathrm{j}\omega_p\mathbb{I}$.

Searching for a steady-state solution of the form (17), in this case we find

$$\Xi(e^{\mathrm{j}\omega_p T}) = -\frac{\Gamma(\mathrm{j}\omega_p)}{\alpha+e^{-\mathrm{j}\omega_p T}B(e^{\mathrm{j}\omega_p T})}. \tag{41}$$

Finally, repeating the steps from eq. (19) to eq. (24), one gets the TF from a line disturbance to the duty cycle,

$$H^d_{v_{\mathrm{in}}}(\mathrm{j}\omega_p) = -\frac{1}{T}\frac{\Gamma(\mathrm{j}\omega_p)(1-e^{-\mathrm{j}\omega_p T_{\mathrm{on}}})}{\alpha+e^{-\mathrm{j}\omega_p T}B(e^{\mathrm{j}\omega_p T})}. \tag{42}$$

This article has been accepted for publication in IEEE Transactions on Circuits and Systems I: Regular Papers. This is the author's version which has not been fully edited and content may change prior to final publication. Citation information: DOI 10.1109/TCSI.2025.3557278

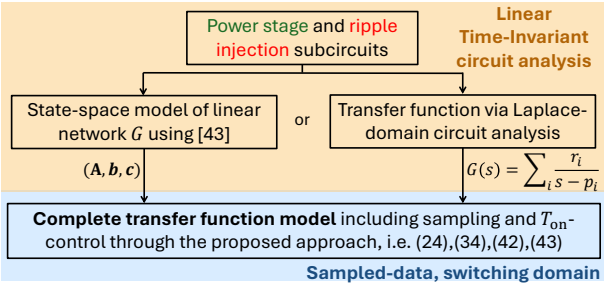

Fig. 3. Logical steps going from the RBCOT converter circuit to the closed-loop TF, taking either the state-space [43] or the TF approach.

Note that, similarly to (34), the coefficient $\Gamma(\mathrm{j}\omega_p)$ can be expressed through the modal realization of $G(s)$ in (33), i.e.

$$\Gamma(\mathrm{j}\omega_p) = \sum_{i=1}^{\nu} \frac{r_i}{(\mathrm{j}\omega_p - p_i)} \frac{1 - e^{(\mathrm{j}\omega_p - p_i)T_{\text{on}}}}{1 - e^{(\mathrm{j}\omega_p - p_i)T}}, \tag{43}$$

that is an expression of $\Gamma(\mathrm{j}\omega_p)$ in terms of poles and residues of the linear network G.

E. Summary of modeling procedure

The main results of the above derivations are the control-to-duty TF $H^d_{v_{\text{ref}}}$ defined by (24) and (30), along with the line-to-duty TF $H^d_{v_{\text{in}}}$ given by (42) and (43).

In practice, to evaluate these closed-loop TFs for a given RBCOT converter, the proposed technique starts by considering the power stage and ripple injection subnetworks as indicated in Fig. 1(a). These are represented by the linear network G defined by (5), that is associated with the TF $H^y_{v_{\text{SW}}}(s)$ from the voltage v_{SW} (at the SW node) to the signal y at the input of the Main Comparator. This linear network is characterized through standard linear network analysis, and Fig. 3 summarizes two alternative ways to proceed. The first (left branch) is to compute a state-space model $(\mathbf{A}, \boldsymbol{b}, \boldsymbol{c})$ through the method outlined in [43]. Alternatively (right branch), Laplace-domain circuit analysis provides the TF $H^y_{v_{\text{SW}}}(s)$.

Once a state-space or TF model of G is found (via either of the methods in Fig. 3), the closed-loop TFs in (24) and (42) that include the COT modulator (with its discrete-time sampling action) are given in exact form. We remark that the COT modulator is often considered the most hard-to-model part because it behavior is event-driven (constrained by (9)).

In practice, the TF $G(s)$ or the state-space $(\mathbf{A}, \boldsymbol{b}, \boldsymbol{c})$ might be cumbersome to compute in exact form without intricate algebraic expressions, so that only approximate low-order expressions might be available. In such case a crucial point is that no further approximation is involved in going from this approximate model of G to the closed-loop TFs.

Conversely, existing works [6], [32] crucially rely on approximations done upfront on the switching waveforms and are not obviously separated from the sampled-data analysis. In fact, [32] is inherently dependent on the straight-line approximation to evaluate the perturbations on the time-domain waveform. In [6], the same approximation is necessary to evaluate the static modulator gain and simplifications are inevitable to evaluate the infinite mathematical series appearing in the model. In other words, a strength of our approach is that potential approximations are done on the LTI TF $G(s)$, thus enabling designers to choose the most convenient simplification (e.g. dominant poles, negligible components) depending on the analysis purposes (e.g. low/high-frequency). Further details on the advantages of the proposed modelling technique over existing RBCOT modelling techniques will be provided in Sec. V-C.

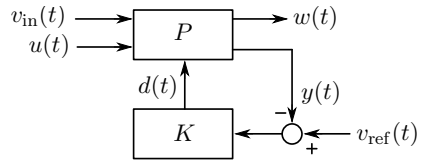

Fig. 4. System-theoretic block diagram of the RBCOT converter in Fig. 1(a).

IV. Complete Small-Signal Model Characterization

The previous sections provided a closed-form expression of two key closed-loop RBCOT TFs, namely the control-to-duty $H^d_{v_{\text{ref}}}$ and the v_{in}-to-duty $H^d_{v_{\text{in}}}$. In this section, we complete the small-signal characterization of the RBCOT Buck converter by deriving closed-loop TFs between other important pairs of network variables, i.e. control-to-output $H^{v_{\text{o}}}_{v_{\text{ref}}}$, the output impedance $Z^{\text{CL}}_{\text{out}}$ and the line-to-output M. This is done by combining the two previous fundamental results (24) and (42) with standard network analysis so that derivations like the ones in Sec. III need not be repeated.

In particular, we consider a generic excitation $u(t)$ injected in the LTI network following the switches (e.g., $u(t)$ might be the load current $\tilde{i}_{\text{out}}(t)$, see Fig.1(b)). Similarly, $w(t)$ is a generic output quantity probed either from the LTI network or the switches pair. The objective of this section is to find the (closed-loop) TF from u to w.

Through the abstraction depicted in Fig. 4, we can view the operation of the RBCOT as the combination of a feedback modulator K, and a network P. The block K represents the sampling action and it controls the duty-ratio based on the error signal $v_e(t) = v_{\text{ref}}(t) - y(t)$. The block P represents both the switches pair $\text{SW}_{0,1}$ and the LTI network comprising the power stage and the ripple injection network, as shown in Fig. 1(a). Note that this representation is consistent with the ones reported in several other works [6], [23].

In the following analysis we will need to relate the voltages at the input and output nodes of the switches $\text{SW}_{0,1}$ of Fig. 1(a). For this purpose, let us recall that

$$v_{\text{SW}}(t) = d(t) v_{\text{in}}(t) \tag{44}$$

where $v_{\text{in}}(t) = V_{\text{in}} + \tilde{v}_{\text{in}}(t)$ is the overall converter input voltage. When studying the small-signal effect of a perturbation on the input (line) voltage, the component $\tilde{v}_{\text{in}}(t) = \hat{v}_{\text{in}} e^{\mathrm{j}\omega_p t}$ is set to an harmonic stimulus at frequency ω_p. Using (44), the harmonic component of $v_{\text{SW}}(t)$ at frequency ω_p (denoted

as $[v_{\rm SW}(t)]_1$) is written in terms of the spectral component of $v_{\rm in}(t)$ and $d(t)$ as follows

$$[v_{\rm SW}(t)]_1 = [d(t)]_1[v_{\rm in}(t)]_0 + [d(t)]_0 \underbrace{[v_{\rm in}(t)]_1}_{=\hat{v}_{\rm in}} \tag{45}$$

where $[d(t)]_1 = \hat{d}(\mathrm{j}\omega_p)$ and $[v_{\rm SW}(t)]_1 = \hat{v}_{\rm SW}(\mathrm{j}\omega_p)$ are the fundamental components of the duty cycle response and the switch output voltage, respectively. The quantities $[v_{\rm in}(t)]_0$ and $[d(t)]_0$ represent the DC components (average values), respectively $V_{\rm in}$ and D, so that

$$\hat{v}_{\rm SW}(\mathrm{j}\omega_p) = V_{\rm in}\hat{d}(\mathrm{j}\omega_p) + D\hat{v}_{\rm in}(\mathrm{j}\omega_p). \tag{46}$$

These equations are consistent with the traditional PWM switch model originally described in [44].

From the abstract description of Fig. 4, the small-signal behavior of the converter can be re-written as

$$\begin{aligned} \hat{d}(\mathrm{j}\omega_p) &= K(\mathrm{j}\omega_p)\left[\hat{v}_{\rm ref}(\mathrm{j}\omega_p) - \hat{y}(\mathrm{j}\omega_p)\right] \\ \hat{y}(\mathrm{j}\omega_p) &= H^y_{v_{\rm SW}}(\mathrm{j}\omega_p)\hat{v}_{\rm SW}(\mathrm{j}\omega_p) + H^y_u(\mathrm{j}\omega_p)\hat{u}(\mathrm{j}\omega_p), \end{aligned} \tag{47}$$

where the term $K(\mathrm{j}\omega_p)$ represents the modulator TF. The output $\hat{w}(\mathrm{j}\omega_p)$ can be written as

$$\hat{w}(\mathrm{j}\omega_p) = H^w_{v_{\rm SW}}(\mathrm{j}\omega_p)\hat{v}_{\rm SW}(\mathrm{j}\omega_p) + H^w_u(\mathrm{j}\omega_p)\hat{u}(\mathrm{j}\omega_p). \tag{48}$$

A. Control-to-Output TF

The closed-loop control-to-output TF $H^{v_o}_{v_{\rm ref}}$ characterizes the output voltage response to variations in $V_{\rm ref}$. Referring to Fig. 1(a), it relates a small-signal perturbation $\hat{v}_{\rm ref}(\mathrm{j}\omega_p)$ to $\hat{v}_o(\mathrm{j}\omega_p)$. This is helpful in designing an outer voltage feedback loop that is typically introduced to guarantee increased accuracy in output voltage regulation.

The closed-loop duty cycle response to $\hat{v}_{\rm ref}(\mathrm{j}\omega_p)$ is given in (24). Combining this with (46), $H^{v_{\rm out}}_{v_{\rm ref}}$ is derived as follows

$$\begin{aligned} H^{v_{\rm out}}_{v_{\rm ref}}(\mathrm{j}\omega_p) &= \frac{\hat{d}(\mathrm{j}\omega_p)}{\hat{v}_{\rm ref}(\mathrm{j}\omega_p)}\frac{\hat{v}_{\rm SW}(\mathrm{j}\omega_p)}{\hat{d}(\mathrm{j}\omega_p)}\frac{\hat{v}_o(\mathrm{j}\omega_p)}{\hat{v}_{\rm SW}(\mathrm{j}\omega_p)} \\ &= H^d_{v_{\rm ref}}(\mathrm{j}\omega_p)V_{\rm in}H^{v_{\rm out}}_{v_{\rm SW}}(\mathrm{j}\omega_p). \end{aligned} \tag{49}$$

B. Output Impedance TF

The output impedance TF $Z^{\rm CL}_{\rm out}(\mathrm{j}\omega_p)$ describes how variations in the load current affect the output voltage. In this case, the input is $\hat{u}(\mathrm{j}\omega_p) = \hat{i}_{\rm out}(\mathrm{j}\omega_p)$. In order to find the duty cycle response we observe that, in (47), the solution $\hat{d}(\mathrm{j}\omega_p)$ is unchanged if we replace $\hat{u}(\mathrm{j}\omega_p)$ with an equivalent perturbation $\hat{v}_{\rm ref,eq}(\mathrm{j}\omega_p) = -H^y_{i_{\rm out}}(\mathrm{j}\omega_p)\hat{i}_{\rm out}(\mathrm{j}\omega_p)$ and set $\hat{u}(\mathrm{j}\omega_p) = 0$. In this way, we find that

$$\hat{d}(\mathrm{j}\omega_p) = -H^d_{v_{\rm ref}}(\mathrm{j}\omega_p)H^y_{i_{\rm out}}(\mathrm{j}\omega_p)\hat{i}_{\rm out}(\mathrm{j}\omega_p). \tag{50}$$

We use (46) to find $\hat{v}_{\rm SW}$ and finally (48) to obtain

$$\begin{aligned} &Z^{\rm CL}_{\rm out}(\mathrm{j}\omega_p) = \frac{\hat{v}_o(\mathrm{j}\omega_p)}{\hat{i}_{\rm out}(\omega_p)} = \\ &= H^{v_{\rm out}}_{i_{\rm out}}(\mathrm{j}\omega_p) - H^{v_{\rm out}}_{v_{\rm SW}}(\mathrm{j}\omega_p)V_{\rm in}H^d_{v_{\rm ref}}(\mathrm{j}\omega_p)H^y_{i_{\rm out}}(\mathrm{j}\omega_p), \end{aligned} \tag{51}$$

where $H^{v_{\rm out}}_{i_{\rm out}}(\mathrm{j}\omega_p)$ is the open-loop output impedance TF, i.e. the impedance seen into the output port of the LTI network, with $\hat{v}_{\rm SW} = 0$ and without feedback.

C. Line-to-Output TF

The line-to-output (or, equivalently, audio-susceptibility) TF $M(\mathrm{j}\omega_p) = {}^{\hat{v}_o(\mathrm{j}\omega_p)}/_{\hat{v}_{\rm in}(\mathrm{j}\omega_p)}$ describes how line voltage fluctuations propagate to the output voltage. Referring to Fig. 1(a), it relates an input voltage perturbation at frequency ω_p, i.e., $\hat{v}_{\rm in}(\mathrm{j}\omega_p)$, and the converter small-signal output voltage $\hat{v}_o(\mathrm{j}\omega_p)$.

The line-to-output TF is derived from (46), (42) and (48), where $\hat{w}(\mathrm{j}\omega_p) = \hat{v}_o(\mathrm{j}\omega_p)$ and only the input signal $\hat{v}_{\rm in}(\omega_p)$ is activated, thus obtaining

$$M(\mathrm{j}\omega_p) = H^{v_{\rm out}}_{v_{\rm SW}}(\mathrm{j}\omega_p)\left(D + V_{\rm in}H^d_{v_{\rm in}}(\mathrm{j}\omega_p)\right). \tag{52}$$

V. Validation of the Proposed Technique

This section validates the modeling strategy proposed in Sec. III in several practical scenarios. In particular, the RBCOT architecture of Fig. 1(b) is taken as a reference validation case.

A. Architectural Description of the RBCOT Converter with Artificial Ripple Injection Network

The RBCOT architecture shown in Fig. 1(b) is extensively exploited in several commercial products [2], [3] due to its advantages in terms of architectural simplicity and improved dynamic performance. It is an implementation of the idealized circuit model presented in [45]–[48], where an AC-coupled emulated inductor current signal is added to the output voltage signal and fed back to the Main Comparator.

The topology in Fig. 1(b) involves the introduction of a ripple injection network that facilitates the use of low-ESR ceramic output capacitors in the power stage. Indeed, the circuit synthesizes and injects an artificial signal by directly integrating the voltage waveform on the switching node `SW` through R_f and C_f. The produced ripple is in-phase with the inductor current $i_L(t)$ and it is propagated to the input of the Main Comparator through the DC-blocking capacitor C_b, which extracts the AC component only. Furthermore, the network is typically designed to entirely propagate the ripple of the output voltage $v_{\rm out}(t)$ on $y(t)$, while the resistances $R_{1,2}$ set the bias voltage of $y(t)$ in order to guarantee that $V_{\rm out} = V_{\rm ref}(R_1/R_2 + 1)$. The amplitude of the overall feedback signal $y(t)$ is chosen to ensure that the capacitive ripple contribution at the input of the Main Comparator is negligible compared to the ripple component in phase with the inductor current signal. This avoids the emergence of the notorious subharmonic instability issue in COT converters [32], [49]–[51]. Note that the power stage here considered and shown in Fig. 1(b) is the most commonly employed in applications, but it could in principle be more complex (e.g., multiple output capacitors, parasitic elements like the winding resistance of the power inductor L_f, etc.).

Various design methodologies have been developed for the RBCOT converter embedding the ripple injection network in Fig. 1(b). We address henceforth an exemplary practical scenario that follows from [2].

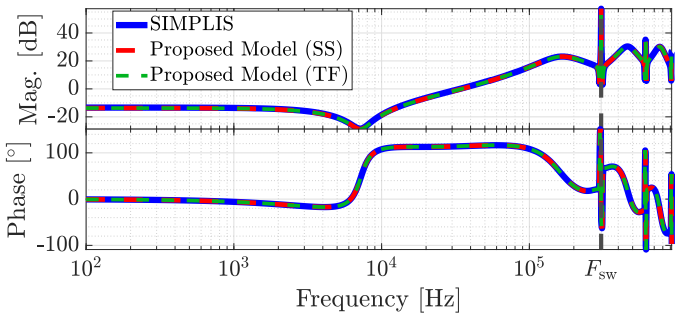

Fig. 5. Closed-loop control-to-duty TF $H^d_{v_{\rm ref}}(s)$.

B. Validation of the Small-Signal Model

We demonstrate the validity of the proposed model on the RBCOT architecture shown in Fig.1(b). At this time, we consider the component values according to the typical application described in [2], namely $L_f = 22\,\mu\text{H}$, $C_{\rm out} = 22\,\mu\text{F}$, $R_{C_{\rm out}} = 10\,\text{m}\Omega$, $R_f = 453\,\text{k}\Omega$, $C_f = 3.3\,\text{nF}$, $C_b = 56\,\text{pF}$, $R_1 = 453\,\text{k}\Omega$, $R_2 = 49.9\,\text{k}\Omega$, $T_{\rm on} = 834\,\text{ns}$, $V_{\rm in} = 48\,\text{V}$, $R_L = 4\,\Omega$ and $V_{\rm ref} = 1.19\,\text{V}$

In the state-space (SS) approach, the LTI subcircuit G is represented by the coefficients $(\mathbf{A}, \boldsymbol{b}, \boldsymbol{c})$. Upon computing them via standard procedures [43], eqs. (24) and (42) directly yield the closed-loop control-to-duty and line-to-duty TFs. Figure 5 demonstrates that the proposed model matches SIMPLIS results both in the low- and high-frequency regions and even beyond $F_{\rm sw}$ (Fig. 5 extends up to $3F_{\rm sw}$). It is important to remark that this TF $H^d_{v_{\rm ref}}$ has no spurious zero at $s = 0$, an issue that affects other models such as [6], [32].

Besides the state-space representation, an alternative way to characterize the LTI subcircuit G is via its TF. For this topology, the following TF is derived in [52] using approximations to simplify the resulting expression

$$H^y_{v_{\rm SW}}(s) = \frac{\hat{y}(s)}{\hat{v}_{\rm SW}(s)} = H_1(s) + H^{v_{\rm out}}_{v_{\rm SW}}(s)H_2(s). \tag{53}$$

In (53), $H^{v_{\rm out}}_{v_{\rm SW}}(s)$ is the power stage TF (from SW to the output node),

$$H^{v_{\rm out}}_{v_{\rm SW}}(s) = \frac{\left(1 + \frac{s}{\omega_{\rm esr}}\right)}{(\frac{s}{\omega_0})^2 + \frac{2\xi_0}{\omega_0}s + 1}, \tag{54}$$

while $H_1(s)$ and $H_2(s)$ are the ripple injection network TFs

$$\begin{aligned} H_1(s) &= \frac{s\tau_b}{(\frac{s}{\omega_1})^2 + \frac{2\xi_1}{\omega_1}s + 1}, \\ H_2(s) &= \frac{R_2}{R_1 + R_2} \cdot \frac{(\frac{s}{\omega_2})^2 + \frac{2\xi_2}{\omega_2}s + 1}{(\frac{s}{\omega_1})^2 + \frac{2\xi_1}{\omega_1}s + 1}. \end{aligned} \tag{55}$$

The newly defined parameters appearing in (54) and (55) are reported in Table I.

Starting from a pole-residue form of (53), the closed-loop control-to-duty TF is evaluated by first computing $B(z)$ according to (34), and then $H^d_{v_{\rm ref}}$ via (24). Similarly, the line-to-duty TF depends on $\Gamma(\text{j}\omega_p)$, that is also expressed in terms of poles and residues of $H^{v_{\rm out}}_{v_{\rm SW}}(s)$ via (43).

The control-to-duty and line-to-duty TFs are sufficient for a complete characterization of the RBCOT, as discussed in Sec. IV. The TFs $H^{v_{\rm out}}_{v_{\rm ref}}(s)$, $Z^{\rm CL}_{\rm out}(s)$, $M(s)$ are given by (49), (51) and (52), respectively. In particular, the evaluation of $Z^{\rm CL}_{\rm out}$ depends on $H^{v_{\rm out}}_{i_{\rm out}}$ and $H^{y}_{i_{\rm out}}$ appearing in (51). For this topology,

$$\begin{aligned} H^{v_{\rm out}}_{i_{\rm out}}(s) &= R_L \parallel \left((sC_{\rm out})^{-1} + R_{C_{\rm out}}\right) \parallel sL_f \\ H^{y}_{i_{\rm out}}(s) &= H^{v_{\rm out}}_{i_{\rm out}}(s)H_2(s). \end{aligned} \tag{56}$$

These three TFs are shown in Fig. 6, which indicates that the proposed model, derived either through the SS or TF approaches, agrees with SIMPLIS simulations. Quantitatively, the maximum error observed in these curves is below 0.25 dB.

TABLE I
PARAMETERS IN (54)- (55) REFERRING TO THE SCHEMATIC IN FIG. 1(B)

Parameter Name	Parameter Value
τ_b	$C_b(R_1 \parallel R_2)$
$\tau_f,\ \tau_b'$	$C_fR_f,\ C_bR_1$
ω_0	$\frac{1}{\sqrt{L_fC_{\rm out}\left(1+\frac{R_{C_{\rm out}}}{R_L}\right)}}$
$\omega_1,\ \omega_2$	$\frac{1}{\sqrt{\tau_b\tau_f}},\ \frac{1}{\sqrt{\tau_b'\tau_f}}$
$\omega_{\rm esr}$	$\frac{1}{R_{C_{\rm out}}C_{\rm out}}$
ξ_0	$\frac{1}{2}\frac{R_{C_{\rm out}}C_{\rm out}+\frac{L_f}{R_L}}{\sqrt{L_fC_{\rm out}\left(1+\frac{R_{C_{\rm out}}}{R_L}\right)}}$
ξ_1	$\frac{1}{2}\left(\sqrt{\frac{\tau_f}{\tau_b}}+\sqrt{\frac{\tau_b}{\tau_f}}+\sqrt{\frac{C_bR_f}{C_fR_1\|\|R_2}}\right)$
ξ_2	$\frac{1}{2}\left(\sqrt{\frac{\tau_f}{\tau_b'}}+\sqrt{\frac{C_bR_f}{C_fR_1}}\right)$

In case algebraic expressions simpler than (53) are desired, the proposed methodology allows exploiting different, more severe, approximations. A possible application-specific alternative is described in the following to showcase the flexibility of this model.

Several applications of the RBCOT converter in Fig. 1(b) require a short load-transient settling time, which is mainly influenced by C_b [2]. The set of component values reported in [2] ensure that this requirement is fulfilled. Specifically, it holds $C_b \ll C_f$, thus enabling the following approximations

$$H_1(s) \approx \frac{1}{\tau_f}\frac{1}{s - \omega_{p0}}, \quad H_2(s) \approx \frac{s - \omega_{z0}}{s - \omega_{p0}}. \tag{57}$$

In (57), we have defined $\omega_{z0} = -(R_1C_b)^{-1}$, and $\omega_{p0} = -((R_fC_f)^{-1} + [C_b(R_1 \parallel R_2)]^{-1})$. In addition, by neglecting the presence of a damping term in (54), $H^{v_{\rm out}}_{v_{\rm SW}}(s)$ becomes

$$H^{v_{\rm out}}_{v_{\rm SW}}(s) \approx \frac{\omega_0^2}{\omega_{\rm esr}}\frac{(s - \omega_{\rm esr})}{(s - \text{j}\omega_0)(s + \text{j}\omega_0)}. \tag{58}$$

Although the resulting expression is inaccurate around the resonant frequency of the power stage low-pass filter ω_0, it is accurate everywhere else.

From (57) and (58), an approximate expression for $H^y_{v_{\rm SW}}$ can be computed as in (53). Using the pole-residue form of

This article has been accepted for publication in IEEE Transactions on Circuits and Systems I: Regular Papers. This is the author's version which has not been fully edited and content may change prior to final publication. Citation information: DOI 10.1109/TCSI.2025.3557278

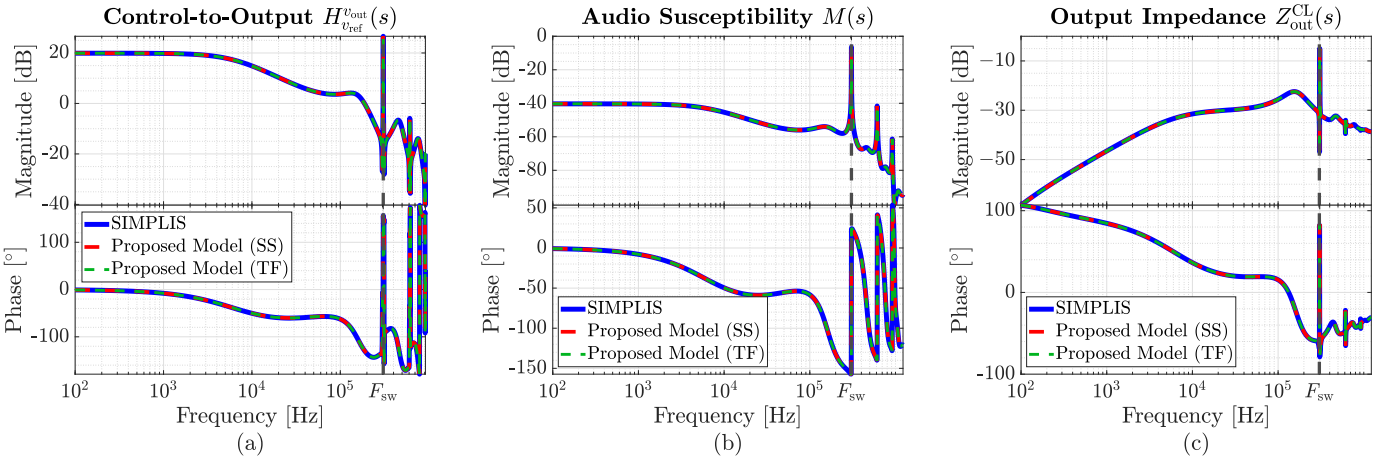

Fig. 6. Validation of the proposed small-signal model of the RBCOT Buck converter in Fig. 1(b) through SIMPLIS simulation results. The model has been computed via both state-space equations and the circuit TF. The set of circuit parameters used is that shown in the typical application described in [2]. 6(a) Control-to-Output TF. 6(b) Line-to-Output TF. 6(c) Output impedance TF.

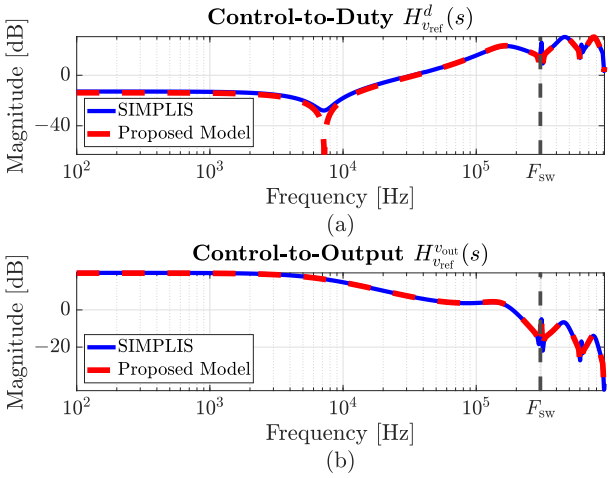

Fig. 7. Comparison between the exact and the approximated small-signal models for the RBCOT Buck converter embedding the ripple injection network shown in Fig. 1(b) and the set of component values in [2]. (a): modulator TF. (b): control-to-output TF.

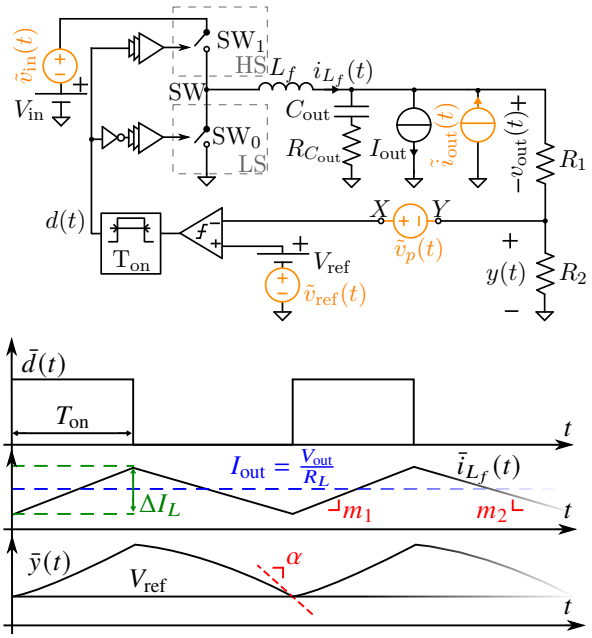

Fig. 8. Buck Converter with V-COT control. Top: schematic, with perturbations (orange) introduced to estimate the closed-loop small-signal TFs. Bottom: Voltage and current waveforms.

this simplified $H^{y}_{v_{SW}}$ in (34), (43) yields the closed-loop TFs. A comparison between the results offered by the approximate models and SIMPLIS simulation results is reported in Fig. 7 where, by way of example, both $H^{d}_{v_{ref}}$ and $H^{v_{out}}_{v_{ref}}$ are shown. Note that, compatibly with the approximation in (58), the former is inaccurate around the resonant frequency ω_0, while the latter is accurate in the whole frequency range.

In the foregoing section, it is shown that previous modeling methods [6], [32] implicitly make use of approximations of this kind, but in an uncontrolled manner. In fact, it is seen that the proposed more general approach yields the model described in [32] as a particular case that is obtained by replacing the exact $H^{y}_{v_{SW}}$ with an high-frequency approximation.

C. Comparison with other modeling approaches

This section provides a comparison against other modeling techniques available in the literature, specifically with [6], [32], [34]. To this aim, the RBCOT architecture in Fig. 8 is taken as a reference in view of its ubiquity. In [32] a closed-loop control-to-duty TF is not explicitly provided since the power stage, switches, and the modulator are treated collectively as a single entity instead of separate blocks. The modeling technique in [32] relies on the DF technique, and it is thus strongly dependent on the examined circuit topology. Indeed, the complexity of the algebraic expressions involved in this modeling process increases prohibitively when additional circuit stages are introduced in the converter control loop (e.g., refer to Fig. 1(b)), thus limiting its generality. Additionally, only the closed-loop control-to-output and the output impedance TFs of the V^2 COT in Fig. 8 are given

This article has been accepted for publication in IEEE Transactions on Circuits and Systems I: Regular Papers. This is the author's version which has not been fully edited and content may change prior to final publication. Citation information: DOI 10.1109/TCSI.2025.3557278

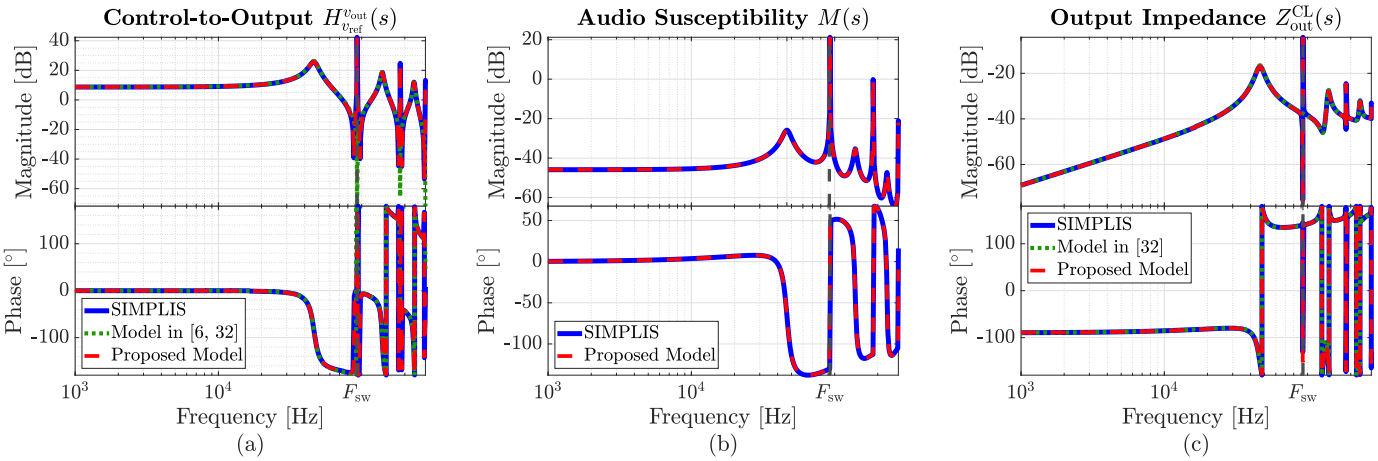

Fig. 9. Comparison between the analytical main closed-loop TF and the SIMPLIS simulation results (blue solid curve) for the V-COT Buck converter in Fig. 8. Both the proposed small-signal model (red dashed curve) and the one described in [6], [32] (green dashdotted curve) are shown. Note that in [6], only the control-to-output TF is provided. It is equivalent to that proposed in [32], where also the output impedance is present. (a) Control-to-Output TF. (b) Line-to-Output TF. (c) Output impedance TF.

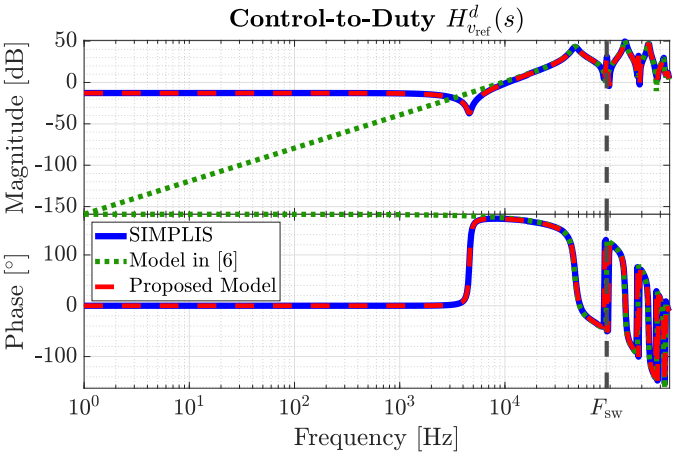

Fig. 10. Comparison between the exact closed-loop control-to-duty TF (24) (proposed, red dashed line), the one from [6] (green dashdotted curve), and SIMPLIS results (blue solid curve) for the V-COT Buck converter in Fig. 8.

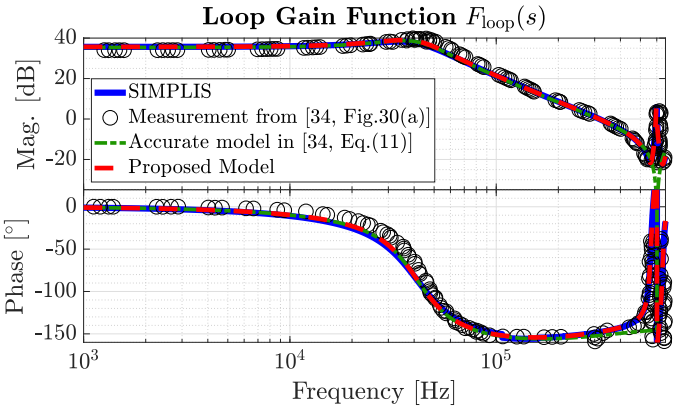

Fig. 11. Comparison between the proposed small-signal model (red line), the accurate model in [34] (green dash-dotted line), the measurement results extracted from [34, Fig. 30(a)] (black circles) and SIMPLIS simulations (blue line).

in [32, Eq. (9) and (12)], while the audio susceptibility TF is not given. Figures 9(a)and 9(c) compare these two TFs with the proposed ones based on the component values and circuit parameters listed in [6, Table II]. Next, we show that the model in [32] is a special case of the one proposed herein.

Let us consider a high-frequency approximation of the $H^{y}_{v_{SW}}$ TF for the Buck converter with V^2 COT control (Fig. 8),

$$H^{y}_{v_{SW}}(s) \approx H_v \left(b_1 s^{-2} + b_2 s^{-1}\right), \tag{59}$$

where $H_v = R_2/(R_1+R_2)$, $b_1 = 1/(L_f C_{out})$ and $b_2 = R_{C_{out}}/L_f$. This is a widely used approximation (see, for instance, both [6], [32]).

Adopting (59) to represent the subnetwork G is equivalent to using its state-space representation

$$\mathbf{A} = (0,\ 0\,;1,\ 0)\,,\ \boldsymbol{b} = \begin{pmatrix} H_v b_1 & H_v b_2 \end{pmatrix}^{\mathrm{T}},\ \boldsymbol{c} = \begin{pmatrix} 0 & 1 \end{pmatrix}. \tag{60}$$

To evaluate (24), we need both $B(z)$ and α. Substituting the coefficients in (30), we get

$$B(z) = V_{in} H_v b_1 T_{on} z (1-z)^{-1}. \tag{61}$$

Note that this approximation precludes us from computing α in (16a) as $\alpha = B(1)$. However, this is estimated by taking advantage of the fact that α is the slope of $\bar{y}$ right before the switching instant at $\bar{t}_k^-$, as per (27). Assuming $y(t) \simeq H_v v_{out}(t)$ (reasonable for practical ripple injection network with high input impedance), an analytical expression of α is computed from the slope of $v_{out}(t)$ at $t = \bar{t}_k^-$. Resorting to the small-ripple approximation [21, Ch. 2.2] depicted at the bottom of Fig. 8, the rising slope of $\bar{i}_{L_f}(t)$ is $m_1 = (V_{in} - V_{out})/L_f$, while its falling slope is $m_2 = -V_{out}/L_f$. The overall ripple of $\bar{i}_{L_f}(t)$ is $\Delta I_L = m_1 T_{on}$. Assuming the AC component of the inductor current flows entirely in C_{out} and $R_{C_{out}}$, i.e. $\bar{i}_{C_{out}}(t) = (\bar{i}_{L_f}(t) - I_{out})$, the output voltage is $\bar{v}_{out}(t) = R_{C_{out}} \bar{i}_{C_{out}}(t) + \bar{v}_{C_{out}}(t)$. Therefore, considering $\bar{i}_{C_{out}}(t) = C_{out} \dot{\bar{v}}_{C_{out}}(t)$, the coefficient $\alpha = H_v \dot{\bar{v}}_{out}(t_k^-)$ reads

$$\alpha = H_v \left(m_2 R_{C_{out}} - \frac{m_1 T_{on}}{2 C_{out}} \right). \tag{62}$$

This article has been accepted for publication in IEEE Transactions on Circuits and Systems I: Regular Papers. This is the author's version which has not been fully edited and content may change prior to final publication. Citation information: DOI 10.1109/TCSI.2025.3557278

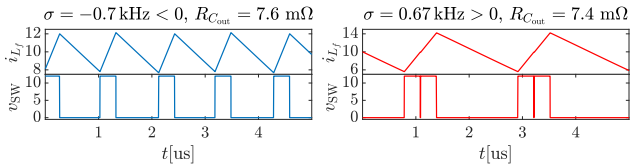

Fig. 12. Emergence of subharmonic instability in the circuit of Fig. 8(top) as observed through transient simulation results in SIMPLIS.

The control-to-duty TF according the proposed model is evaluated by replacing the expressions (61), (62), along with the well-known CCM voltage conversion ratio [14, Ch.2] $V_{\text{out}}/V_{\text{in}} = T_{\text{on}}/T$ in (24),

$$H^d_{v_{\text{ref}}}(s) = \frac{-(H_v m_2 T)^{-1}\left(1-e^{-sT}\right)\left(1-e^{-sT_{\text{on}}}\right)}{\left(1+\frac{T-T_{\text{on}}}{2C_{\text{out}}R_{\text{out}}}\right)-\left(1-\frac{T+T_{\text{on}}}{2C_{\text{out}}R_{C_{\text{out}}}}\right)e^{-sT}}. \tag{63}$$

We wish to compare (63) with [32], which only gives the control-to-output TF ${}^{v_{\text{out}}}\!/_{v_{\text{ref}}} = ({}^{d}\!/_{v_{\text{ref}}})({}^{v_{\text{out}}}\!/_{d})$. The transfer function in [32, Eq. (9)] can be written as

$$\frac{\hat{v}_{\text{out}}(s)}{\hat{v}_{\text{ref}}(s)} = \frac{\hat{d}(s)}{\hat{v}_{\text{ref}}(s)}\frac{\hat{v}_{\text{out}}(s)}{\hat{d}(s)} = \frac{\hat{d}(s)}{\hat{v}_{\text{ref}}(s)}V_{\text{in}}\frac{\hat{v}_{\text{out}}(s)}{\hat{v}_{\text{SW}}(s)}. \tag{64}$$

The last factor ${}^{\hat{v}_{\text{out}}(s)}\!/_{\hat{v}_{\text{SW}}(s)}$ is the TF from v_{SW} to the output voltage and can be expressed as

$$\frac{\hat{v}_{\text{out}}(s)}{\hat{v}_{\text{SW}}(s)} = \frac{sC_{\text{out}}R_L+1}{s^2L_fC_{\text{out}}L_f}\left(R_L \parallel \left(R_{C_{\text{out}}}+\frac{1}{sC_{\text{out}}}\right)\right). \tag{65}$$

The TF in (65) appears explicitly as a factor in [32, Eq. (9)]. Hence, based on (64), we observe that the remaining factor appearing in [32, Eq. (9)], that is ${}^{\hat{d}(s)}\!/_{\hat{v}_{\text{ref}}(s)}$, is exactly equal to (63) derived with the proposed model (with $H_v = 1$). Hence, the model in [32] is implicitly based on the high-frequency approximation of $H^y_{v_{\text{SW}}}(s)$ in (59), and so it is a particular case of the proposed more general model.

Furthermore, we can also derive the output impedance given in [32, Eq.(12)] through the proposed model (51). In fact, using the approximate TF $H^{v_{\text{out}}}_{i_{\text{out}}}(s) = H^y_{i_{\text{out}}}(s) \approx R_{C_{\text{out}}} + (sC_{\text{out}})^{-1}$ together with (63) and (65) in (51) yields the same equation as [32, Eq.(12)].

The proposed model allows to predict the emergence of subharmonic instability. In fact, it can be shown that if $R_{C_{\text{out}}}C_{\text{out}} < T_{\text{on}}/2$, $H^d_{v_{\text{ref}}}(s)$ in (63) has unstable poles. The poles of (63) are aligned on a vertical line in the complex plane [26], all with the same real part σ. Fig. 12 shows the time-domain simulation results corresponding to stable and unstable conditions.

Other related models are presented in [6], [8], where all the main stages of the converter architecture are directly mapped into a small-signal equivalent. According to that approach, a two-step strategy is proposed, consisting in *a)* computation of the static modulator gain F_m (formally defined in [8, Eqs. (2), (4) and (5)]), and *b)* analytical or numerical evaluation of a mathematical series including all the replicas of $H^y_{v_{\text{SW}}}(s)$ [6, Eqs. (7), (16)]. Step *b)* is a non-negligible limitation, as it requires computing a non-trivial mathematical series. This brings the need to derive a simplified form of the $H^y_{v_{\text{SW}}}$ TF (see [6, Eqs. (9) and (17)]), with an unavoidable impact on the accuracy of the final result. Also, evaluating an analytic expression of F_m becomes cumbersome for complex topologies (e.g., the one in Fig. 1(b)), and it further requires approximations in order to estimate the slopes of the signals around the sampling instant.

A small-signal model for the V-COT Buck converter shown in Fig. 8 is found in [6], where $H^y_{v_{\text{SW}}}(s) = H_v H^{v_{\text{out}}}_{v_{\text{SW}}}(s)$. From the main results given therein (specifically, from [6, Table III] and the block diagram in [6, Fig. 4]), the closed-loop control-to-duty TF is derived as

$$H^d_{v_{\text{ref}}}(s) = \frac{F_m(1-e^{-sT_{\text{on}}})}{1+F_mH_vV_{\text{in}}\phi(s)}, \tag{66}$$

with $\phi(s) \triangleq \sum_{k=-\infty}^{+\infty} H^{v_{\text{out}}}_{v_{\text{SW}}}(s-\frac{\text{j}2\pi k}{T})(1-e^{(\text{j}\frac{2\pi}{T}k-s)T_{\text{on}}})$. This is here compared with the proposed model and SIMPLIS results in Fig. 10 using the component values in [6, Table II]. Also in this case, the actual evaluation of the model in (66) is infeasible without assuming a simplified expression for $H^{v_{\text{out}}}_{v_{\text{SW}}}(s)$, that appears in the series. In particular, an high-frequency approximation similar to (65) is the key to obtain a manageable closed-form expression in [6]. In addition, the slopes needed for computing the F_m coefficient in (66) are derived through the straight-line approximation.

In Fig. 10, we provide a comparison between the control-to-duty TFs obtained with the proposed model, with [6] and through SIMPLIS. It is clearly visible that (66) is inaccurate in the low-frequency range as a result of the approximations used in [6, Eq.(17)] and [8, Eq.(32)]. In particular, the evaluation of (66) through steps *a)* and *b)* relies on high-frequency approximations that are inadequate at low frequency. Consequently, the SIMPLIS simulation results shows a finite and non-zero static gain of the closed-loop control-to-duty TF, while the model [6] has a spurious zero for $s \to 0$.

Concerning the control-to-output TF, also presented in [6], a different low-frequency behavior is observed. This TF is computed as in (49) exploiting an approximate $H^{v_{\text{out}}}_{v_{\text{SW}}}$ (see [6, Eq. (17)]), and the corresponding results are compared with SIMPLIS in Fig. 9(a). Intriguingly, despite the inaccuracy of the control-to-duty TF, the model matches the numerical simulation. This is because the low-frequency asymptotic behavior of the approximate duty-to-output TF (a double pole at $s = 0$) compensates the zeros at $s = 0$ of the control-to-duty TF. Note that, unlike the complete model described herein, only the control-to-output TF is derived in [6]. Finally, Fig. 9(a) confirms that the approach of [6] leads to the same result as [32], a fact also shown in [6, Appendix I].

Moreover, we also compare the proposed model with the one presented in [34], which presents a technique to analytically derive the loop gain of RBCOT Buck converters. Specifically, referring to Fig. 8(top), the loop gain TF is defined as $F_{\text{loop}}(s) = v_Y(s)/v_X(s)$. The loop gain is related to the closed-loop TF $H^{v_{\text{out}}}_{v_{\text{ref}}}$. In fact, it holds $F_{\text{loop}}(s) = H^{v_{\text{out}}}_{v_{\text{ref}}}(s)/(1-H^{v_{\text{out}}}_{v_{\text{ref}}}(s))$, a familiar relationship arising in feedback control systems [21, Ch.9] corresponding to unity feedback gain $H_v = 1$. The measured samples of $F_{\text{loop}}(s)$ are extracted from [34, Fig.30(a)] and used to validate the proposed model. The RBCOT topology under study is the one

in Fig. 8(top). The results are shown in Fig. 11, suggesting a good correlation with measurements.

To sum up, this comparison with previous modeling techniques [6], [32], [34] shows that the proposed flow allows a complete and exact dynamical characterization of any RBCOT converter, regardless of the architectural complexity and without the need for approximations to be imposed at the beginning of the derivation phase. This ensures the validity of the model across the entire frequency range, enabling the analysis of both slow and fast-scale phenomena, as well as system loop gain relevant for evaluating bandwidth and stability margins.

VI. Conclusion

In conclusion, an exact and complete sampled-data modeling approach for RBCOT Buck converters is proposed that provides all relevant converter TFs. The formal derivation of the model is validated through SIMetrix/SIMPLIS simulations as well as experimental measurements. Finally, a comparative analysis with other modeling techniques is performed.

References

[1] W. Z. Nancy Zhang, Wenkai Wu, "D-cap™ mode with all-ceramic output capacitor application," Texas Instruments, Tech. Rep., February 2011, sLVA453.

[2] *LM5013 100-V Input, 3.5-A Non-Synchronous Buck DC/DC Converter with Ultra-Low IQ*, Texas Instruments, October 2022, initial release.

[3] *NB638 High Efficiency, Fast Transient, 7A, 28V Synchronous Step-down Converter in a Tiny 3x4mm QFN Package*, Monolithic Power Systems (MPS), October 2017, rev.1.19.

[4] R. Redl and J. Sun, "Ripple-based control of switching regulators—an overview," *IEEE Trans. on Power Electronics*, vol. 24, no. 12, pp. 2669–2680, 2009. doi: 10.1109/TPEL.2009.2032657

[5] W.-C. Liu, C.-H. Cheng, P. P. Mercier, and C. C. Mi, "Small-signal analysis and design of constant on-time controlled buck converters with duty-cycle-independent quality factors," *IEEE Trans. on Power Electronics*, vol. 38, no. 7, pp. 8379–8393, 2023. doi: 10.1109/TPEL.2023.3268613

[6] N. Yan, X. Ruan, and X. Li, "A general approach to sampled-data modeling for ripple-based control—part ii: Constant on-time and constant off-time control," *IEEE Trans. on Power Electronics*, vol. 37, no. 6, pp. 6385–6396, 2022. doi: 10.1109/TPEL.2021.3132624

[7] S. Sridhar and Q. Li, "Multiphase constant on-time control with phase overlapping—part i: Small-signal model," *IEEE Trans. on Power Electronics*, vol. 39, no. 6, pp. 6703–6720, 2024. doi: 10.1109/TPEL.2024.3368343

[8] N. Yan, X. Ruan, and X. Li, "A general approach to sampled-data modeling for ripple-based control—part i: Peak/valley current mode and peak/valley voltage mode," *IEEE Trans. on Power Electronics*, vol. 37, no. 6, pp. 6371–6384, 2022. doi: 10.1109/TPEL.2021.3132619

[9] X. Cheng, J. Liu, and Z. Liu, "A generalized multifrequency small-signal model for high-bandwidth buck converters under constant-frequency voltage-mode control," *IEEE Trans. on Power Electronics*, vol. 35, no. 8, pp. 8186–8199, 2020. doi: 10.1109/TPEL.2019.2961682

[10] E. Figueres *et al.*, "Adaptive two-loop voltage-mode control of dc-dc switching converters," *IEEE Trans. on Industrial Electronics*, vol. 53, no. 1, pp. 239–253, 2006. doi: 10.1109/TIE.2005.862254

[11] S. C. Smithson and S. S. Williamson, "A unified state-space model of constant-frequency current-mode-controlled power converters in continuous conduction mode," *IEEE Trans. on Industrial Electronics*, vol. 62, no. 7, pp. 4514–4524, 2015. doi: 10.1109/TIE.2015.2412514

[12] A. Elserougi, I. Abdelsalam, A. Massoud, and S. Ahmed, "A non-isolated hybrid-modular dc-dc converter for dc grids: Small-signal modeling and control," *IEEE Access*, vol. 7, pp. 132 459–132 471, 2019. doi: 10.1109/ACCESS.2019.2941249

[13] B. Choi, W. Lim, S. Bang, and S. Choi, "Small-signal analysis and control design of asymmetrical half-bridge dc-dc converters," *IEEE Trans. on Industrial Electronics*, vol. 53, no. 2, pp. 511–520, 2006. doi: 10.1109/TIE.2006.870715

[14] D. Maksimovic and R. Zane, "Small-signal discrete-time modeling of digitally controlled pwm converters," *IEEE Trans. on Power Electronics*, vol. 22, no. 6, pp. 2552–2556, 2007. doi: 10.1109/TPEL.2007.909776

[15] H. Li *et al.*, "A describing function-based stability analysis method for cascaded dc-dc converters," *IEEE Open Journal of the Industrial Electronics Society*, vol. 3, pp. 484–495, 2022. doi: 10.1109/OJIES.2022.3191906

[16] F. Wu, S. Fan, and S. Luo, "Small-signal modeling and closed-loop control of bidirectional buck-boost current-fed isolated dc–dc converter," *IEEE Trans. on Industrial Electronics*, vol. 68, no. 5, pp. 4036–4045, 2021. doi: 10.1109/TIE.2020.2984448

[17] J. Y. Zhu and B. Lehman, "Control loop design for two-stage dc-dc converters with low voltage/high current output," *IEEE Trans. on Power Electronics*, vol. 20, no. 1, pp. 44–55, 2005. doi: 10.1109/TPEL.2004.839872

[18] R. D. Middlebrook and S. Cuk, "A general unified approach to modelling switching-converter power stages," in *1976 IEEE Power Electronics Specialists Conference*, 1976, pp. 18–34. doi: 10.1109/PESC.1976.7072895

[19] V. Mummadi and B. K. Mohan, "Robust digital voltage-mode controller for fifth-order boost converter," *IEEE Trans. on Industrial Electronics*, vol. 58, no. 1, pp. 263–277, 2011. doi: 10.1109/TIE.2010.2044130

[20] M. Veerachary, "Analysis of minimum-phase fourth-order buck dc–dc converter," *IEEE Trans. on Industrial Electronics*, vol. 63, no. 1, pp. 144–154, 2016. doi: 10.1109/TIE.2015.2472525

[21] R. Erickson and D. Maksimović, *Fundamentals of Power Electronics*. Springer International Publishing, 2020.

[22] S. Amir, R. van der Zee, and B. Nauta, "An improved modeling and analysis technique for peak current-mode control-based boost converters," *IEEE Trans. on Power Electronics*, vol. 30, no. 9, pp. 5309–5317, 2015. doi: 10.1109/TPEL.2014.2368176

[23] F. Tan and R. Middlebrook, "A unified model for current-programmed converters," *IEEE Trans. on Power Electronics*, vol. 10, no. 4, pp. 397–408, 1995. doi: 10.1109/63.391937

[24] H. Li *et al.*, "High-order generalized averaging method for power electronics modeling from dc to above half the switching frequency," *IEEE Trans. on Power Electronics*, vol. 40, no. 1, pp. 176–194, 2025. doi: 10.1109/TPEL.2024.3450712

[25] X. Cheng, J. Liu, Y. Shao, and Z. Liu, "High-frequency modelling of constant on-time current mode buck converter and controller design by combining genetic algorithm," *IEEE Trans. on Power Electronics*, vol. 37, no. 12, pp. 15 099–15 110, 2022. doi: 10.1109/TPEL.2022.3197768

[26] A. R. Brown and R. Middlebrook, "Sampled-data modeling of switching regulators," in *1981 IEEE Power Electronics Specialists Conference*, 1981, pp. 349–369. doi: 10.1109/PESC.1981.7083659

[27] R. Ridley, "A new, continuous-time model for current-mode control (power convertors)," *IEEE Trans. on Power Electronics*, vol. 6, no. 2, pp. 271–280, 1991. doi: 10.1109/63.76813

[28] J. Sun, "Small-signal modeling of variable-frequency pulsewidth modulators," *IEEE Trans. on Aerospace and Electronic Systems*, vol. 38, no. 3, pp. 1104–1108, 2002. doi: 10.1109/TAES.2002.1039428

[29] R. Middlebrook, "Describing function properties of a magnetic pulsewidth modulator," *IEEE Trans. on Aerospace and Electronic Systems*, vol. AES-9, no. 3, pp. 386–398, 1973. doi: 10.1109/TAES.1973.309724

[30] V. Vorperian, R. Tymerski, and F. Lee, "Equivalent circuit models for resonant and pwm switches," *IEEE Trans. on Power Electronics*, vol. 4, no. 2, pp. 205–214, 1989. doi: 10.1109/63.24905

[31] J. Li and F. C. Lee, "New modeling approach and equivalent circuit representation for current-mode control," *IEEE Trans. on Power Electronics*, vol. 25, no. 5, pp. 1218–1230, 2010. doi: 10.1109/TPEL.2010.2040123

[32] J. Li and F. C. Lee, "Modeling of v^2 current-mode control," *IEEE Trans. on Circuits and Systems I: Regular Papers*, vol. 57, no. 9, pp. 2552–2563, 2010. doi: 10.1109/TCSI.2010.2043018

[33] Y.-R. Huang and C.-J. Chen, "A novel describing function small-signal modeling approach for passive ripple constant on-time controlled converter with exponentially varying slope," *IEEE Trans. on Power Electronics*, vol. 39, no. 7, pp. 8425–8435, 2024. doi: 10.1109/TPEL.2024.3383855

[34] D. Lu, X. Zeng, and Z. Hong, "Accurate loop gain model of ripple-based constant on-time controlled buck converters," *IEEE Trans. on Power Electronics*, vol. 38, no. 6, pp. 7034–7048, 2023. doi: 10.1109/TPEL.2023.3254906

[35] C. Li *et al.*, "Small-signal modeling and loop analysis of ultrafast series capacitor trans-inductor voltage regulator with constant on-time control," *IEEE Trans. on Power Electronics*, vol. 40, no. 2, pp. 3262–3274, 2025. doi: 10.1109/TPEL.2024.3488734

[36] Y.-C. Lin, C.-J. Chen, D. Chen, and B. Wang, "A ripple-based constant on-time control with virtual inductor current and offset cancellation for dc power converters," *IEEE Trans. on Power Electronics*, vol. 27, no. 10, pp. 4301–4310, 2012. doi: 10.1109/TPEL.2012.2191799

[37] C. V. Ioan Stoichita, Matthew Weng, "Constant on-time regulator with internal ripple generation and improved output voltage accuracy," U.S. Patent US20 080 088 292A1, April 17, 2008.

[38] I. Stoichita, "Ripple generation in buck regulator using fixed on-time control to enable the use of output capacitor having any esr," U.S. Patent US7 482 793B2, January 27, 2009.

[39] P. Nora, "Current sharing method for cot buck converter," U.S. Patent US20 140 375 288A1, December 15, 2015.

[40] J. Grobe *et al.*, "Monolithic integration of a 400v gan half-bridge converter with output voltage regulation," *IEEE Trans. on Circuits and Systems II: Express Briefs*, vol. 71, no. 10, pp. 4591–4595, 2024. doi: 10.1109/TCSII.2024.3398783

[41] Y. Yan, F. C. Lee, S. Tian, and P.-H. Liu, "Modeling and design optimization of capacitor current ramp compensated constant on-time v^2 control," *IEEE Trans. on Power Electronics*, vol. 33, no. 8, pp. 7288–7296, 2018. doi: 10.1109/TPEL.2017.2766259

[42] R. Horn and C. Johnson, *Topics in Matrix Analysis*, ser. Topics in Matrix Analysis. Cambridge University Press, 1994.

[43] L. Chua, C. Desoer, and E. Kuh, *Linear and Nonlinear Circuits*, ser. Electrical & electronic engineering. McGraw-Hill, 1987.

[44] V. Vorperian, "Simplified analysis of pwm converters using model of pwm switch. continuous conduction mode," *IEEE Trans. on Aerospace and Electronic Systems*, vol. 26, no. 3, pp. 490–496, 1990. doi: 10.1109/7.106126

[45] W.-C. Liu, C.-J. Chen, C.-H. Cheng, and H.-J. Chen, "A novel accurate adaptive constant on-time buck converter for a wide-range operation," *IEEE Trans. on Power Electronics*, vol. 35, no. 4, pp. 3729–3739, 2020. doi: 10.1109/TPEL.2019.2936524

[46] J.-P. He *et al.*, "A voltage ripple compensation method for constant on-time buck converter," *IEEE Access*, vol. 11, pp. 139 628–139 642, 2023. doi: 10.1109/ACCESS.2023.3342016

[47] C.-J. Chen *et al.*, "A novel ripple-based constant on-time control with virtual inductor current ripple for buck converter with ceramic output capacitors," in *2011 Twenty-Sixth Annual IEEE Applied Power Electronics Conference and Exposition (APEC)*, 2011, pp. 1488–1493. doi: 10.1109/APEC.2011.5744789

[48] W.-W. Chen *et al.*, "A novel quick response of rbcot with vic ripple for buck converter," *IEEE Trans. on Power Electronics*, vol. 28, no. 9, pp. 4299–4307, 2013. doi: 10.1109/TPEL.2012.2212461

[49] J.-P. He *et al.*, "A voltage ripple compensation method for constant on-time buck converter," *IEEE Access*, vol. 11, pp. 139 628–139 642, 2023. doi: 10.1109/ACCESS.2023.3342016

[50] J. Wang, J. Xu, and B. Bao, "Analysis of pulse bursting phenomenon in constant-on-time-controlled buck converter," *IEEE Trans. on Industrial Electronics*, vol. 58, no. 12, pp. 5406–5410, 2011. doi: 10.1109/TIE.2011.2123861

[51] J. Wang *et al.*, "Dynamical effects of equivalent series resistance of output capacitor in constant on-time controlled buck converter," *IEEE Trans. on Industrial Electronics*, vol. 60, no. 5, pp. 1759–1768, 2013. doi: 10.1109/TIE.2012.2190956

[52] M. Lin, T. Zaitsu, T. Sato, and T. Nabeshima, "Frequency domain analysis of fixed on-time with bottom detection control for buck converter," in *IECON 2010 - 36th Annual Conference on IEEE Industrial Electronics Society*, 2010, pp. 481–485. doi: 10.1109/IECON.2010.5674981